Role of electrical synapses in multidimensional population activity of Golgi cell network in cerebellar cortex

A Thesis submitted to

Indian Institute of Science Education and Research Pune in partial fulfilment of the requirements for the BS-MS Dual Degree Programme

by

Mahima Gautam

Indian Institute of Science Education and Research Pune
Dr. Homi Bhabha Road,
Pashan, Pune 411008, INDIA.

Date: 15th March, 2024
Under the guidance of
Supervisor: Rishikesh Narayanan,
Professor IISc Bangalore
From June 2023 to March 2024
INDIAN INSTITUTE OF SCIENCE EDUCATION AND RESEARCH PUNE

Certificate

This is to certify that this dissertation entitled 'Role of Electrical Synapses in Multidimensional Population Activity of Golgi Cell Network in Cerebellar Cortex' towards the partial fulfilment of the BS-MS dual degree programme at the Indian Institute of Science Education and Research, Pune, represents study/work carried out by Mahima Gautam at Indian Institute of Science Bangalore under the supervision of Rishikesh Narayanan, Professor, Molecular Biophysics Unit, during the academic year 2023-2024.

Rishikesh Narayanan

Committee:

Name of your Guide: Rishikesh Narayanan

Name of Your TAC: Collins Assisi

This thesis is dedicated to Ammi Abba

Table of Contents

Declaration

I hereby declare that the matter embodied in the report entitled 'Role of Electrical Synapses in Multidimensional Population Activity of Golgi Cell Network in Cerebellar Cortex' are the results of the work carried out by me at the Molecular Biophysics Unit at Indian Institute of Science, Bangalore, under the supervision of Professor Rishikesh Narayanan and the same has not been submitted elsewhere for any other degree. Wherever others contribute, every effort is made to indicate this clearly, with due reference to the literature and acknowledgement of collaborative research and discussions.

Mahima Gautam

Name: Mahima Gautam
Roll no.: 20191064
Date: 15th March 2024

List of figures

List of tables

Acknowledgements

"*We* are the *sum* of *all people we have ever met*; *you change* the *tribe* and the *tribe changes you*."

- Dirk Wittenborn

I will always be indebted to Prof Rishikesh Narayanan, Sir, who gave me a place in his lab to work on this project. I knew nothing before I came to this lab and he taught me everything from the scratch (quite literally, by writing things in my notebook and giving me initial lectures). His NPP (Neuronal Physiology and Plasticity) lectures taught me to think about literature critically and rigorously and to ask questions. I also got to meet some wonderful people while I was at the lab: Anjana unni, who answered my silliest of doubts and kept me fed, Sanjana didi and Sarang bhaiya who helped me out with NEURON and MPMOSS (and of course Sarang bhaiya's expertise in MATLAB), Richa didi who taught me *'not knowing things now is okay but not knowing them ever is not'* and Barnopriyo, my bench mate who was always supportive and encouraged me. All the lab meeting and computational meets not only helped me to learn how to present and think about a paper and made progress in my work but also gave me confidence to stand and present something in front of people. At this place, I grew not only as a student but also as a person.

I am grateful to my past mentors and supervisors, Raghav sir, Madhusudhan sir, Shikha didi and Mukundan bhaiya, who inspired and supported me during my previous projects. I would also like to mention VK Sahu sir and my other teachers from school who inspired me to pursue science in the first place. Thank you to Vaishanavi Tiwari, Anuradha and all my other friends to whom I can turn to for support anytime. I am also very grateful to all the people who were there for me when I caught dengue: Sakshi, Sir and labmates, Mona aunty, Supdeepta and Anya.

I am and always will be thankful to my family- the people I love the most in this entire multiverse, and who give me strength and support to do everything good in my life. Mummy & Papa are the reason because of whom I am doing any of this and who made sure that I'm getting the best of things in this world. Bitti, Mahi & Babu, three angels of my life, are the people for whom I am doing everything. Any of this wouldn't have been possible without you guys. To them, I owe all.

Abstract

Inhibitory neuronal network of Golgi cells (GoCs) connected with gap junctions (GJs) in cerebellum display multiple modes during spontaneous behaviour. A network-wide modulation of GoC activity that occurs at a slow pace is correlated with the level of whisking and locomotion. On the other hand, a faster population activity that arises from heterogeneous GoC responses mixed in space is responsible for encoding more precise information. By constructing a biologically detailed circuit model of GoC, it was possible to reproduce the observed common population mode and the distributed modes. However, these properties were no longer present when electrical coupling was eliminated. The strength and variability of electrical synaptic connections between GABAergic interneurons play a crucial role in determining spike synchrony within neuronal networks. The electrical transmission of spike afterhyperpolarization serves as a critical factor in enabling oscillatory population synchronization, allowing rhythmic firing to occur even in the presence of significant heterogeneities.

However, the mechanism behind the multidimensional population activity of GoCs still remains unclear. To this end, we simulated physiologically realistic and morphologically reduced models of GoCs connected with GJs. We used MPMOSS, a stochastic search algorithm, to generate 40-parameter randomized models spanning 14 active and passive ion channels biophysically constraint by their localization profiles and gating kinetic to search for valid cerebellar GoC models. The models that fell in the range of 14 sub- and supra- threshold cellular-scale electrophysiological measurements of cerebellar GoCs of rats were considered as valid models. We got 486 valid models out of 50,000 generated models that were electrophysiologically valid, manifested heterogeneity, as their biological counterparts, and were widespread throughout the parametric space thus displaying degeneracy. We then connected valid GoCs with GJs to characterize the two cell-network. Our results show that low pass filtering of signal, due to the RC circuit, as it traverses GJs and its resonance at low frequency could be the responsible for the manifestation of multidimensional population activity of GoCs. Low pass filtering creates a virtual compartment that can confine distinct activity within a subset of GoCs and resonance at low frequency may allow network-wide synchronization of GoC activity.

Contributions

Contributor name	Contributor role
Mahima Gautam	Conceptualization Ideas
Prof Rishikesh Narayanan	Methodology
Mahima Gautam	Software
Mahima Gautam	Validation
Mahima Gautam	Formal analysis
Mahima Gautam	Investigation
Mahima Gautam	Resources
Mahima Gautam	Data Curation
Mahima Gautam	Writing - original draft preparation
Mahima Gautam	Writing - review and editing
Mahima Gautam	Visualization
Prof Rishikesh Narayanan	Supervision
Prof Rishikesh Narayanan, IISER Pune	Project administration
-	Funding acquisition

Chapter 1: Introduction

> *"We have a brain for one reason and one reason only - that's to produce adaptable and complex movements. Movement is the only way we have affecting the world around us… I believe that to understand movement is to understand the whole brain. And therefore, it's important to remember when you are studying memory, cognition, sensory processing, they're there for a reason, and that reason is action."*
>
> *- Daniel Wolpert, Neuroscientist, Columbia University*

The brain is a part of the central nervous system responsible for multiple things like learning, memory, communication, processing/ integration of information, abstract thinking, emotions, sensations, and responding to sensory information through movements. Movement is one of the prominent ways to affect the outside environment. It is a result of synergy between the nervous system and the musculoskeletal system. Things ranging from flight, swimming, running, and climbing to speech, writing, hand gestures, and facial expressions are all mediated through muscle contraction. Sensation, memory, and cognitive processes play a role in either driving or suppressing future movements.

In the larval form, Sea quirt, an invertebrate, swims freely in the sea and is equipped with a basic sensory and motor system. At some point in life, it implants on a rock to become sessile for the remainder of its life and digests its nervous system. In essence, complex movements demand the nervous system and that movement is the most essential function of the brain due to which it came into existence (Daniel Wolpert: The real reason for brains, 2011).

1.1 Neural centres responsible for movement

The regulation of movement is governed by neural centres, which are broadly categorized into four separate yet closely interconnected subsystems: lower motor neurons, upper motor neurons, basal ganglia, and cerebellum (**Figure 1.1**). The lower motor neurons comprise the initial subsystem, positioned within the ventral horn of the spinal cord's gray matter and within the motor nuclei of the cranial nerves situated in the brainstem. They transmit their axons from the brainstem and spinal cord to innervate the skeletal muscles of the head and body. The lower motor neurons are crucial in transmitting instructions for movement, whether they are reflexive or voluntary, directly to the muscles. They form circuits promoting coordination between different muscle groups, enabling organized movement. The cell bodies of the upper motor neurons, which comprise the second motor subsystem, are situated in the brainstem or cerebral cortex. These neurons send their axons downward to form synapses with the local circuit neurons. The upper motor neuron pathways play a essential role in orchestrating the planning and initiation of voluntary movements and the execution of intricate spatiotemporal sequences involved in skilled activities.

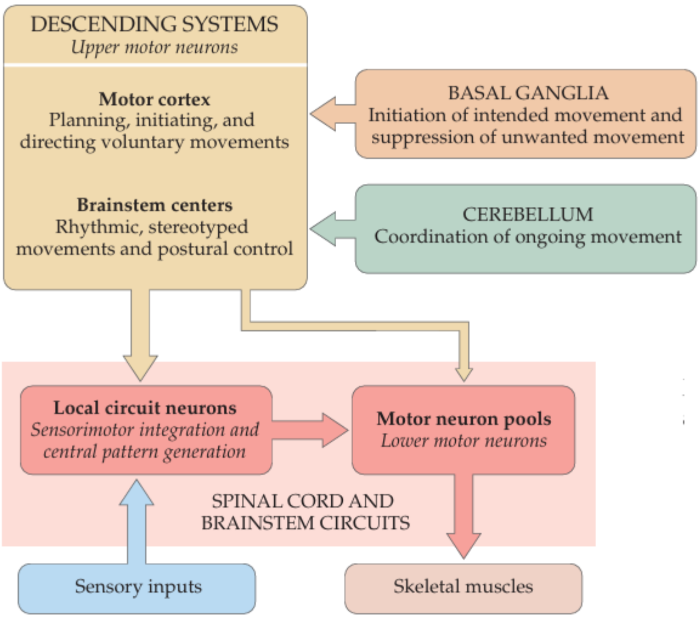

Figure 1.1: Organisation of neural structures involved in movement initiation and control *(Neuroscience, Purves et al., 6th ed, Chapter 16)*.

The basal ganglia and cerebellum constitute the third and fourth subsystems, respectively. They exert control over movement indirectly through modulation of the activity of upper motor neurons situated in the cerebral cortex and brainstem. The basal ganglia are a collection of structures nestled within the depths of the forebrain. The basal ganglia inhibit the initiation of undesired movements by upper motor neurons while priming the motor circuits to execute intended movements. The cerebellum is situated over the pons and the fourth ventricle within the posterior section of the cranium. Through its efferent pathways to the upper motor neurons, the cerebellum detects and attenuates differences between intended movements and those actually executed, thereby facilitating error correction in motor coordination. The cerebellum acts like a fine-tuning machine, constantly reducing errors in the movements, both as they happen and over time (Neuroscience, Purves et al., 6th ed, Chapter 16). Studies have also shown its involvement in cognition and emotion (Leiner *et al.*, 1986).

1.2 Cerebellum

The cerebellum comprises two primary gray matter structures: a layered cortex covering its surface and clusters of cells located within nuclei embedded deep in the white matter of the cerebellum. The cerebellar cortex can be divided into three primary regions based on the sources from where they get input: the cerebrocerebellum, spinocerebellum, and vestibulocerebellum. The cerebrocerebellum primarily resides in the lateral portion of the cerebellar hemisphere and receives input indirectly from numerous regions dispersed throughout the cerebral cortex. The spinocerebellum is situated in the median and paramedian regions of the cerebellar hemispheres and is the sole area that directly receives input from the spinal cord. The lateral region of the spinocerebellum primarily focuses on coordinating movements of distal muscles, while the central strip primarily coordinates movements of proximal muscles and also regulates specific types of eye movements. The vestibulocerebellum, the phylogenetically oldest part of the cerebellum, consists of caudal-inferior lobes and structures like the flocculus and nodulus. It receives signals from the vestibular nuclei in the brainstem and is mainly involved in coordinating the vestibule-ocular reflex and regulating movements essential for maintaining balance and posture. The cerebellar peduncles bridge connections between the cerebellum and other regions of the nervous system.

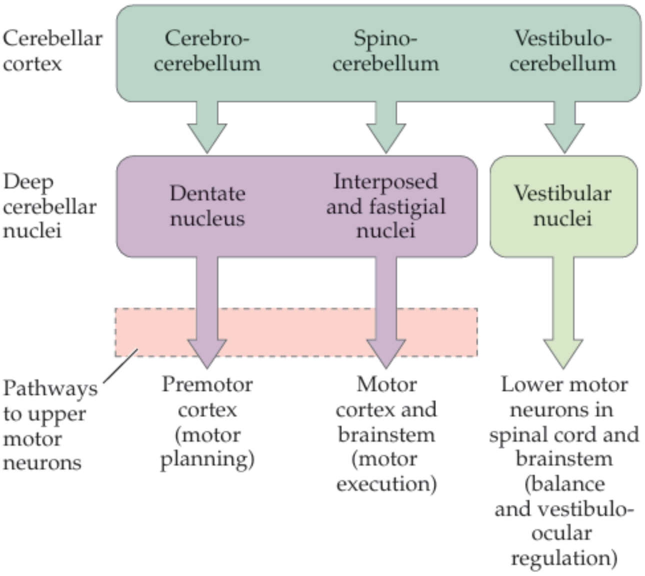

Figure 1.2: Organisation of cerebellar areas and their projections to other regions responsible for motor movement *(Neuroscience, Purves et al., 6th ed, Chapter 20)*.

The cortical neurons project to the cerebellum by synapsing onto the pontine nuclei. The entire cerebellum is also subject to modulatory inputs originating from the inferior olivary nucleus in the medulla oblongata. These inputs are involved in the learning and memory processes performed by the circuitry within the cerebellum. Neurons within the cerebellar cortex extend projections to the deep cerebellar nuclei (DCN) and the vestibular complex. DCN gives the ultimate output of the cerebellar circuit. These structures send projections to upper motor neurons located in the brainstem and to thalamic nuclei that connect with upper motor neurons within the motor cortex. Each hemisphere of the cerebellum has four main deep nuclei: the dentate nucleus, two interposed nuclei, and the fastigial nucleus. Each of these nuclei receives input from distinct areas of the cerebellar cortex. (**Figure 1.2**; Neuroscience, Purves et al., 6th ed, Chapter 20).

1.3 Cerebellar circuit

The cerebellar cortex is organized into three layers: the molecular layer (ML), the Purkinje cell layer (PCL), and the granular layer (GL; **Figure 1.3**). The cerebellum receives its primary input through two main pathways: mossy fibres (MFs) and climbing fibres (CFs). They both give excitatory inputs to the downstream cells and use glutamate as their neurotransmitter. The MF input carries a diverse array of sensory and motor information that originates from various nuclei within the brainstem and spinal cord. Within the GL, MFs form excitatory synaptic connections onto granule cells (GrCs). The axons of GrCs ascend vertically towards the ML, where they bifurcate to create T-shaped branches referred to as parallel fibres (PFs; Pijpers *et al.*, 2006; Oberdick and Sillitoe, 2011). PF synapse onto a distinct cell type called Purkinje

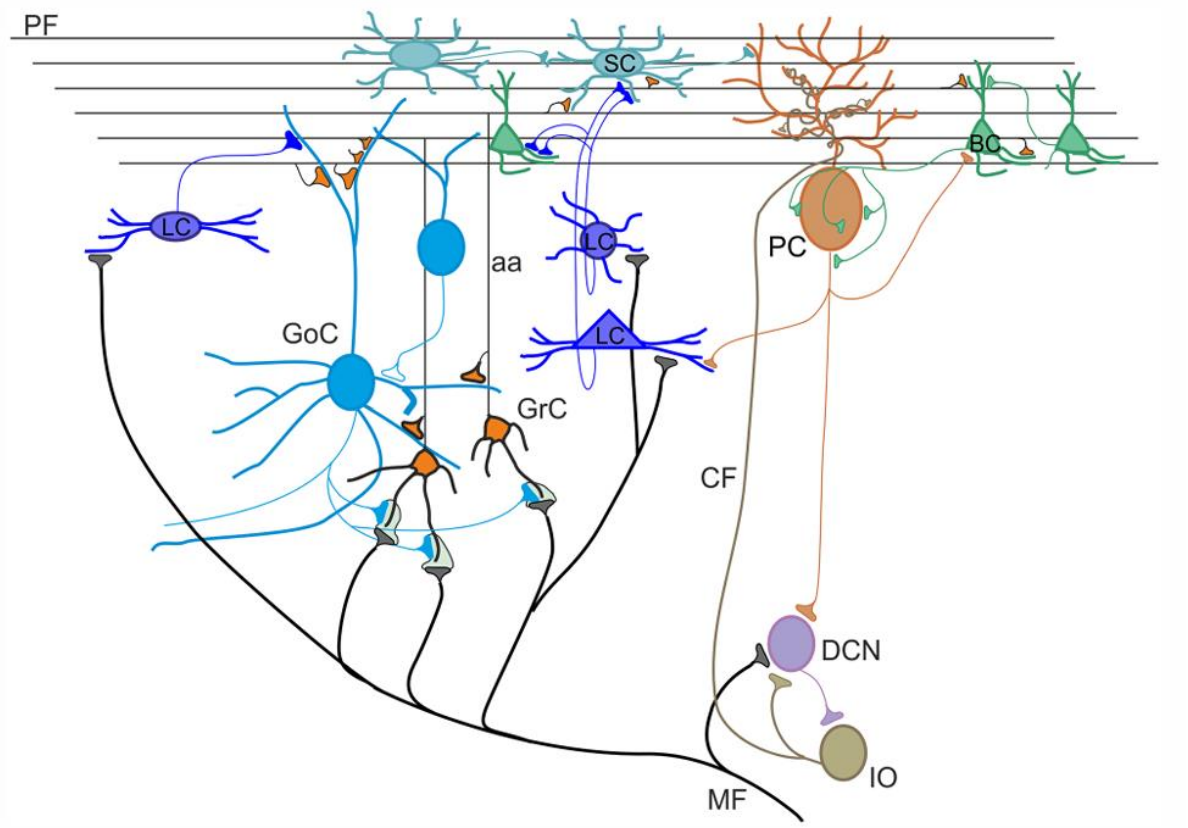

Figure 1.3: Schematic representation of cerebellar circuit *(Prestori* et al., *2019)*.

cells (PCs), which are GABAergic in nature. The PCs are the ultimate destination for all incoming pathways to the cerebellar cortex and receive excitatory inputs from PF and CF. Each PF makes excitatory synapses onto dendrites of hundreds of PCs. The CFs originating from the inferior olive make multiple contacts to a single PC, thus giving it a strong excitatory input. PCs, in turn, make inhibitory synapses onto DCN. Neurons within DCN also receive excitatory synaptic connections from collateral branches of both MFs and CFs. (Ito, 2013; Ito *et al.*, 2014). The CFs deliver a "training" signal that regulates the synaptic strength of the connection between PFs and PCs. (Neuroscience, Purves et al., 6th ed, Chapter 20).

The inhibitory control of PCs on the DCNs is regulated by local inhibitory circuits formed by basket cells (BCs) and stellate cells (SCs) within the ML. (Crook *et al.*, 2007; Witter *et al.*, 2016). Two types of interneurons with a mixed glycinergic/GABAergic phenotype exist in the GL. These interneurons are known as Lugaro cells (LCs) and Golgi cells (GoCs), which indirectly regulate the outgoing activity of PCs. The axons of LCs make contact with the soma and dendrites of BCs and SCs in the ML. Furthermore, through collaterals, LC axons constitute a significant input to GoCs (Dieudonné and Dumoulin, 2000). GoCs are the principal inhibitory neurons of the granule cell layer and provide inhibition to GrCs. GoCs receive excitatory inputs from MFs and PFs and inhibitory inputs from LCs, SCs, BCs and other GoCs (Eccles *et al.*, 1966; Dieudonné, 1998; Kanichay and Silver, 2008; Cesana *et al.*, 2013). MFs and ascending granule cell axons (aa) synapse onto the basal dendrites, and PFs synapse onto the apical dendrites of GoCs (Cesana *et al.*, 2013).

The presynaptic terminals of MFs are present within a structure called glomerulus. Glomerulus is enclosed within a glial sheath and contains MF terminal with hundreds of active zones, dendrites of ~50 GrCs, a few GoCs, unipolar brush cells and LCs (Eccles *et al.*, 1966; Palay and Chan-Palay, 1974; Jakab and Hámori, 1988; Xu-Friedman and Regehr, 2003). This is, thus, the site of both MF-mediated excitation and GoC-mediated inhibition. GrCs also experience tonic inhibition arising from activity at "shared" synapses due to the lingering of neurotransmitters within the glomerulus (Brickley *et al.*, 1996). The glomerulus also behaves as a filter that increases the signal-to-noise ratio of the excitatory input from MFs to the PC by inhibiting GrCs not concurrently excited by multiple MFs or not excited by a favoured pattern (Chan-Palay and Palay, 1971).

1.4 Cerebellar Golgi cell

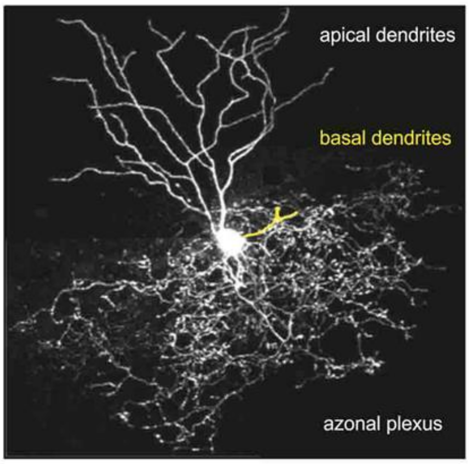

Figure 1.4: Confocal microscopy reconstruction of GoC *(D'Angelo* et al.*, 2013)*.

GoCs are the primary inhibitory interneuron in the granule cell layer. The network formed by these interneurons regulates the information transfer within the cerebellar cortex's input layer. These interneurons possess typically round or polygonal soma, varying in size from 10 to 30 µm. They also exhibit an extensive axonal plexus within the granule cell layer (**Figure 1.4**), allowing them to inhibit thousands of granule cells through both direct synaptic connections and the spillover of GABA within the glomerulus (Brickley *et al.*, 1996; Rossi and Hamann, 1998). The basolateral dendrites of GOCs receive input from aa of GrCs, and the basal dendrites of GoCs that go into the glomerulus receive excitatory input from MF. Apical dendrites extending into the molecular layer receive excitatory inputs from PF originating from GrCs (Dieudonné, 1998; Cesana *et al.*, 2013). Thus, GoCs are involved in both feedforward and feedback inhibition onto GrCs. Most GoCs exhibit spontaneous firing at frequencies ranging from 4 to 12 Hz in the presence of synaptic blockers because of intrinsic currents (Forti *et al.*, 2006). They form connexin-36 mediated gap junctions (GJs) between dendrites of adjacent GoCs (Dugué *et al.*, 2009; Vervaeke *et al.*, 2010; Szoboszlay *et al.*, 2016). There is variability in the coupling strength among GoCs, which decreases as the distance between them increases. (Dugué *et al.*, 2009; Vervaeke *et al.*, 2010; Szoboszlay *et al.*, 2016). The activity of GoCs *in vivo* is influenced by sensory inputs (Vos *et al.*, 1999; Holtzman *et al.*, 2006; Barmack and Yakhnitsa, 2008; Xu and Edgley, 2008), sensorimotor activity (Edgley and Lidierth, 1987; van Kan *et al.*, 1993; Prsa *et al.*, 2009; Heine *et al.*, 2010) and cortical UP/DOWN states (Roš *et al.*, 2009).

GoCs display a large afterhyperpolarization (AHP), leading to a significant refractory period. This extended refractory period has the potential to constrain their maximum firing rates, even in the presence of strong excitatory inputs. GoCs can be classified into different neurochemical subtypes depending on their expression of synaptic receptors and signalling molecules. (Geurts *et al.*, 2001; Simat *et al.*, 2007). The majority of GoCs (approximately 65%) are both GABAergic and glycinergic, in addition to expressing metabotropic glutamate receptors (mGluR2) on their dendrites. A smaller proportion (around 15%) of GoCs are solely GABAergic, expressing neurogranin. These cells typically have large soma and are distributed in the deeper layers. Postsynaptic AMPAR primarily facilitates the excitation of GoCs by MFs, which leads to the generation of EPSCs characterized by fast kinetics (Kanichay and Silver, 2008). Excitation of GrCs and GoCs is facilitated by both AMPARs and NMDARs, leading to EPSCs with slower decay kinetics. These signals attenuate as they travel towards the soma due to dendritic filtering. (Watanabe and Nakanishi, 2003).

1.5 Membrane properties and intrinsic excitability of GoC

GoCs display various electro-responsive properties, encompassing phenomena such as spontaneous firing, resonance, phase-resetting, and response patterns marked by rebounds and adaptations in response to depolarizing and hyperpolarizing inputs. Experiments conducted in slices have revealed regular beating of GoCs at approximately 6Hz, along with an increase in spike frequency and precision when repetitively depolarized at the same frequency (Dieudonné, 1998; Forti *et al.*, 2006; Solinas *et al.*, 2007a, 2007b). Upon injection of hyperpolarising current, GoCs produce sagging inward rectification, followed by rebound bursts upon returning to the baseline membrane potential level. In contrast, when these cells are depolarized, they exhibit repetitive discharge with spike-frequency adaptation. This is followed by a hyperpolarizing rebound after the burst upon returning to the baseline membrane potential level. Interestingly, GoCs reset their discharge phase after a burst, starting a new pacing cycle following a pause that accurately aligns with the oscillatory period.

Recent findings utilizing two-photon glutamate uncaging alongside dendritic patch-clamp recordings have demonstrated that GoCs act as passive cables. They provide distance-dependent sublinear synaptic integration and attenuation of distal excitatory inputs. In distal dendrites, there is a greater concentration of GJs, which significantly contributes to membrane conductance (Dugué *et al.*, 2009; Szoboszlay *et al.*, 2016).

The intrinsic electrical properties of GoCs have been experimentally investigated and subsequently modelled using a specific set of ionic channels, as described below: (**Figure 1.5**; Dieudonné, 1998; Afshari *et al.*, 2004; Forti *et al.*, 2006; Solinas *et al.*, 2007a, 2007b, 2010):

(1) *Low-frequency spontaneous firing*: Spontaneous firing relies on the action of four ionic currents, I_h (slow inward-rectifier H-current), $I_{Na\text{-}p}$ (persistent Na current), $I_{K\text{-}AHP}$ (Ca-dependent K current of the SK type), and $I_{K\text{-}slow}$ (slow K current of the M-type): I_h drives the membrane potential into the spontaneous firing region, where the interaction among $I_{Na\text{-}p}$/$I_{K\text{-}AHP}$/$I_{K\text{-}slow}$ facilitates spontaneous firing.

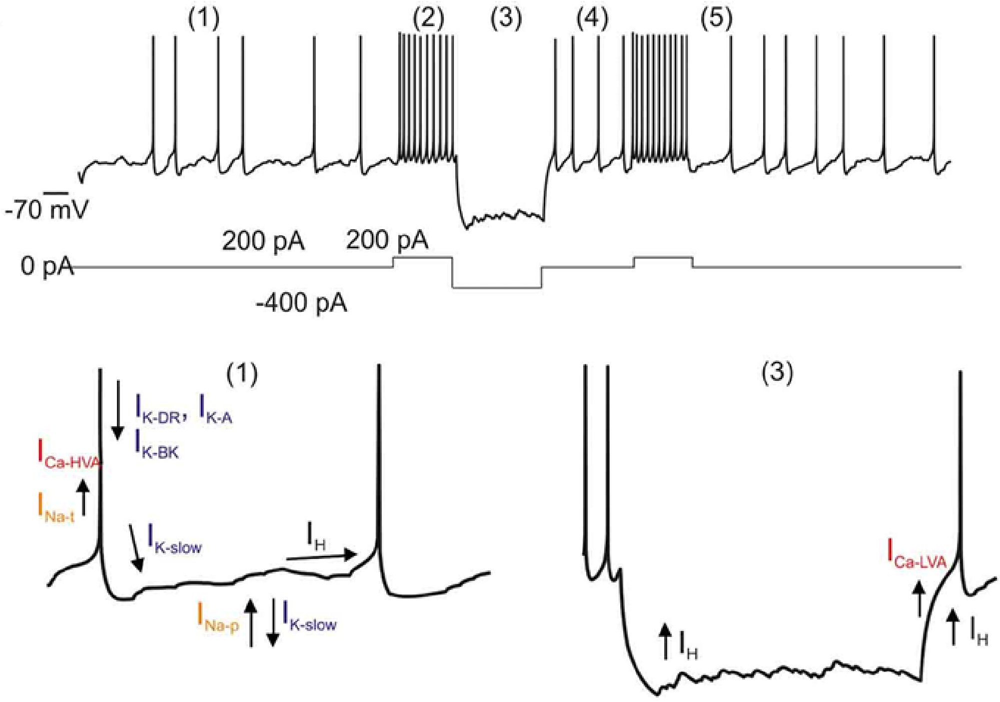

Figure 1.5: Characteristic electrophysiological properties of GoCs and the ionic conductances involved in them *(D'Angelo* et al., *2013)*.

(2) *High-frequency spike discharge upon current injection*: Firing frequency upon current injection is governed by the interaction of the $I_{Na\text{-}t}$ (Transient Na current)/I_{KV} (delayed-rectifier K current) system and is further regulated by the $I_{K\text{-}BK}$ / $I_{Ca\text{-}HVA}$ system.

(3) *Sagging inward rectification*: Both I_h and $I_{Ca\text{-}LVA}$ (low-voltage-activated Ca current) produce rebound excitation after hyperpolarizing current injection.

(4) *Post-inhibitory rebound*: Burst response after hyperpolarization is amplified by $I_{Na\text{-}r}$ (resurgent Na current) and delayed by $I_{K\text{-}A}$ (fast-inactivating K current of the A-type). This burst is succeeded by spike frequency adaptation produced by the interplay of the $I_{Ca\text{-}HVA}$ / $I_{K\text{-}AHP}$ system and $I_{K\text{-}slow}$.

(5) *Phase resetting:* Phase resetting is intricately connected to the calcium-dependent modulation of K currents. Through its coupling with $I_{K\text{-}BK}$ (Ca-dependent K current of

the BK-type), $I_{Ca\text{-}HVA}$ (high-voltage-activated Ca current) increases the fast phase of spike AHP, thus resetting the spiking mechanism and maintaining high-frequency discharge.

Dendritic GJs facilitate dendritic integration and communication within the inter-neuronal network.

1.6 Motivation

People have studied this GABAergic interneuron at cellular scale but our understanding of its dynamics at the population level remains limited. In a recent study conducted by Gurnani and Silver (2021), using random-access 3D two-photon microscopy on awake-behaving mice, they demonstrated that the electrically coupled GoC network exhibits multidimensional population activity. They focused on two distinct cerebellar lobules characterized by differences in their input composition, evolutionary background, and function: Crus I/II in the cerebellar hemisphere, known in rodents for primarily processing whisking and other orofacial sensorimotor inputs, and lobule (Lob) IV/V in the cerebellar vermis, responsible for receiving inputs from the spinocerebellar tract and contributing to posture and locomotion.

This multidimensional population activity consisted of a common mode and a distributed mode. Common mode is the slow widespread modulation of GoC activity in the network, which correlates with the overall behavioural states of whisking and locomotion (**Figure 1.6A**). Clusters of individual GoCs scattered across the local circuit

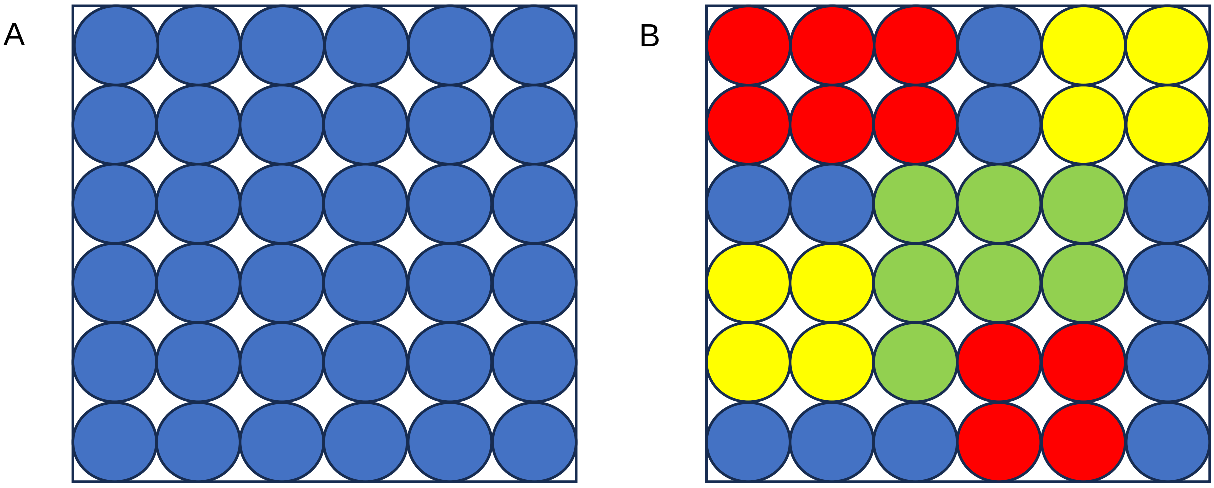

Common mode

carry overall behavioural state, eg. whisking, locomotion

Distributed mode

carry specific behavioural information, eg. paw lift

Figure 1.6: Illustration of common and distributed modes.

also demonstrate distinct dynamics on faster timescales (<1 s) referred to as distributed mode. This differential population activity, resulting from spatially mixed heterogeneous GoC responses, encrypts more precise information such as paw lift. The differential population modes were also shown to be neither global nor clustered (**Figure 1.6B**). The most striking feature of this network is that the common and distributed modes operate independently without interfering with each other.

When GoCs were electrically coupled via GJs in a biologically detailed circuit model, the characteristics of GoC population dynamics could be replicated. Elimination of GJs desynchronized GoC spiking, indicating that electrical coupling between GoCs could support multidimensional activity of GoC network (Gurnani and Silver, 2021). Presence of common and distributed modes in the GoC circuit might facilitate pattern separation and temporal processing, the major proposed functions of GrC layer (Marr, 1969; Albus, 1971; Cayco-Gajic and Silver, 2019). This motivated us to ask what causes the presence of two different independent modes, common and distributed modes, to occur in a network connected with gap junctions.

Previous studies have also shown that the strength and variability of electrical synaptic connections among GABAergic interneurons play crucial role in determining spike synchrony within neuronal networks (Szoboszlay *et al.*, 2016). Combining experiments and modelling, people have also shown that electrical transmission of the spike AHP is important for achieving oscillatory population synchronization. Despite strong heterogeneities, there is emergence of rhythmic firing where its frequency is tuned by the average excitatory input to Golgi cells. Moreover, the modelled network demonstrated marked resonance when stimulated by oscillating inputs (Dugué *et al.*, 2009). Thus, study of GoCs connected via GJs becomes a key to understanding the mechanisms behind multidimensional population activity of GoC network.

In this project, we are interested in looking into the mechanisms which cause this phenomenon in a network of heterogeneous models with dendrites and how this contributes to pattern separation and temporal processing at the level of GrC layer. To address this question, we modelled physiologically realistic and morphologically reduced GoCs with dendrites and connected them with electrical synapses.

Chapter 2: Methods and Materials

We employed a conductance-based multi-compartmental model of Golgi cells (GoCs) with reduced morphology. Each model cell has a soma (20 μm × 10 μm), an axonal initial segment - AIS (2 μm × 1 μm), an axon (100 μm × 1 μm), three basal dendrites (80 μm × 1 μm) and three apical dendrites (200 μm × 2 μm). Apical dendrites are the dendrites located in the molecular layer and basal dendrites are the dendrites contained in granular cell layer. The measurement of each compartment and the number of dendrites is approximated using a detailed morphology of cerebellar GoC, which was uploaded to NeuroMorpho.org (**Figure 2.1**, Masoli *et al.*, 2020). As a part of this study's objective was to construct an intrinsic heterogeneous model population of GoCs for integration into a network, we opted not to employ morphologically realistic models. This decision was made to minimize the computational complexity of individual neurons. GoC models used in this study have active dendrites and are connected with gap junctions (GJ) unlike the previous studies where either only the ionic mechanisms were distributed throughout the GoC structure or the ion channels were restricted only to somatic compartment.

2.1 Passive and Active Neuronal Properties

Passive properties of GoCs were defined using specific membrane capacitance (C_m), axial resistivity (R_a), leak conductance (R_m) and reversal potential of leak (E_{rev}). The specific membrane capacitance was set constant at 1μF/cm^2 across the entire neuron. We inserted thirteen different active channel conductance into the model: resurgent sodium (Nav1.6), delayed rectified potassium (Kv1.1), inactivating KDR (Kv3.4), A-type potassium (Kv4.3), M-type potassium (Kv7.x), big-conductance calcium-activated potassium channel (Kca1.1), middle-conductance calcium-activated potassium channel (Kca3.1), small-conductance calcium-activated potassium channel (Kca2.2), high-voltage-activated calcium (Cav2.2), medium-voltage-activated calcium (Cav2.3), low- voltage-activated calcium (Cav3.1) and two hyperpolarization-activated cyclic nucleotide-gated non-specific cation (HCN1 and HCN2) channels (**Figure 2.1**). To maintain iso-potential conditions within each compartment the neuronal model was compartmentalized based to the d_λ rule (Carnevale and Hines, 2006). Temperature of all the compartments were set to 25 ˚C for simulations as q10 used in mod files of ion channels was derived for temperature range of 20-25 ˚C.

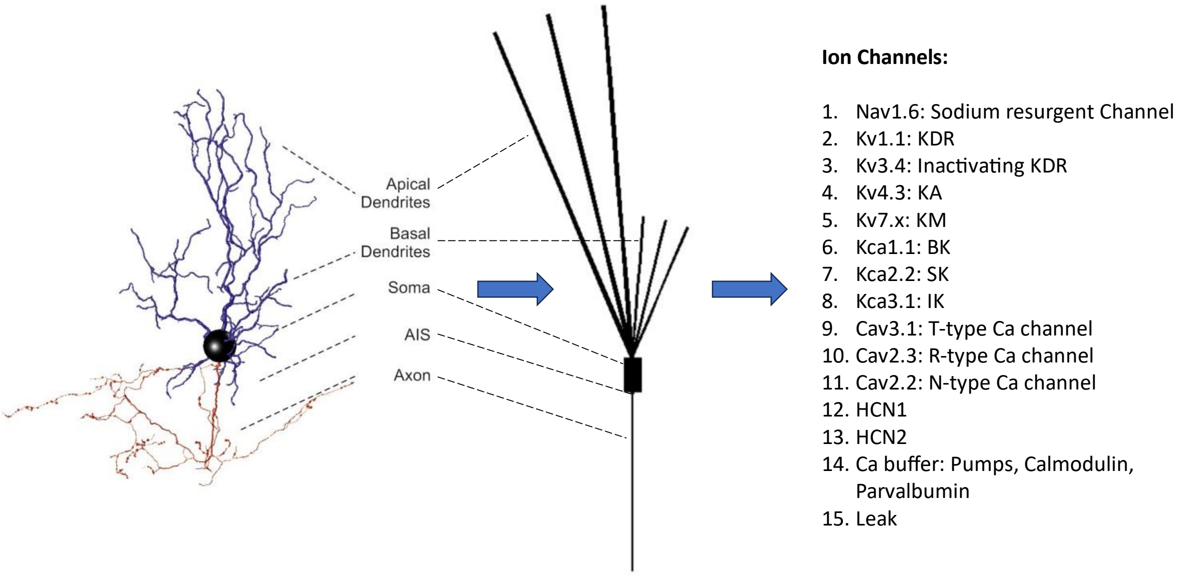

Ion Channels:

1. Nav1.6: Sodium resurgent Channel
2. Kv1.1: KDR
3. Kv3.4: Inactivating KDR
4. Kv4.3: KA
5. Kv7.x: KM
6. Kca1.1: BK
7. Kca2.2: SK
8. Kca3.1: IK
9. Cav3.1: T-type Ca channel
10. Cav2.3: R-type Ca channel
11. Cav2.2: N-type Ca channel
12. HCN1
13. HCN2
14. Ca buffer: Pumps, Calmodulin, Parvalbumin
15. Leak

Figure 2.1: Schematic representation of GoC model and ion channels present in them. Left: 3D morphological reconstruction of GoC, centre: Morphology of GoC mode, right: ion channels inserted into the GoC model. The approximated dimensions and number of compartments of a GoC model is based on the morphology of experimentally determined reconstructed GoC.

All the channels used in the model followed Hodgkin-Huxley formulation, with the exception of the sodium resurgent, BK, SK channels which were implemented using multi-state Markovian kinetics model. Sodium, potassium, and HCN channel currents were computed using the ohmic formulation, while calcium channels followed the Goldman-Hodgkin-Katz (GHK) formulation for current computation. The reversal potentials for Na^{+}, K^{+}, and HCN channel were set to +60 mV, -80 mV, and -20 mV, respectively. Calcium buffer containing Parvalbumin and Calmodulin was incorporated into the model along with calcium pumps. Ion channel distribution and mechanisms are taken from Masoli et al. 2020. The gating mechanism and kinetics of ion channels used were previously validated and used in Granule cell (GrC), Purkinje cell (PC) and GoC models. Distribution of ion channels is according to the electrophysiological data in literature.

2.2 Ion Channel Description

In channels utilizing the Hodgkin-Huxley formulation, the model advanced through adjustments to one or two gating particles, where each gating particle adhered to first-order kinetics as described below:

$$\frac{dm}{dt} = \frac{m_\infty - m}{\tau_m}$$

Where m_∞ and τ_m represented the steady-state value and the time constant of the state variable regulating the gating particle, respectively. Based on corresponding experimental measurements, channel gating and kinetics were adjusted to account for temperature dependence.

The delayed rectifier potassium channel (Kv1.1): The KDR model was adapted from Akemann *et al*. (2009), and the current flowing through this potassium channel was:

$$I = gn^4(V - E_k)$$

The activation gating particle was governed by the following equations:

$$\alpha_n = 0.12889\,\exp(-\frac{V + 45}{-33.90877})$$

$$\beta_n = 0.12889\,\exp\,(-\frac{V + 45}{12.42101})$$

$$n_\infty = \frac{\alpha_n}{\alpha_n + \beta_n}$$

$$\tau_n = \frac{1}{qt\;(\alpha_n + \beta_n)}$$

where $qt = 2.7^{(T-22)/10}$, for temperature T

The inactivating KDR (Kv3.4): The inactivating KDR model was adapted from Khaliq *et al*. (2009), and the current flowing through this potassium channel was:

$$I = gm^3h(V - E_k)$$

The activation gating particle was defined by:

$$m_\infty = \frac{1}{1 + \exp\,(\frac{-V + 24}{15.4})}$$

$$\tau_m = 1000 * \frac{\left(3.4225e^{-05} + 0.00498 * \exp\left(-\frac{v}{-28.29}\right)\right) * 3}{qt}, \qquad if\ v < -35,$$

$$= 1000 * \frac{0.00012851 + \frac{1}{\exp\left(\frac{v+100.7}{12.9}\right) + \exp\left(\frac{v-56}{-23.1}\right)}}{qt}, \quad otherwise$$

The inactivation gating particle was defined by:

$$h_\infty = 0.31 + \frac{0.69}{1 + \exp\,(\frac{V + 5.802}{11.2})}$$

$$\tau_h = 1000 * \frac{(0.0012 + 0.0023 * \exp(-0.141 * v))}{qt}, \qquad if\ v > 0,$$

$$= 1000 * \frac{1.2202e^{-05} + 0.012 * \exp\left(-\left(\frac{Vm-(-56.3)}{49.6}\right)^2\right)}{qt}, \qquad otherwise$$

where $qt = 3^{(T-37)/10}$, for temperature T

The A-type potassium channel (Kv4.3): The KA model was adapted from Diwakar *et al*. (2009), and the current flowing through this potassium channel was:

$$I = ga^3b(V - E_k)$$

The activation gating particle was defined by the following equations:

$$a_\infty = \frac{1}{1 + \exp\,(\frac{V + 38}{-17})}$$

$$\tau_a = \frac{1}{q10 * 0.8147 * \frac{1}{\exp\left(\frac{v + 9.17203}{-23.32708}\right) + 1} + q10 * 0.1655 * \frac{1}{\exp\,(\frac{v + 18.27914}{19.47175})}}$$

The inactivation gating particle was defined by the following equations:

$$b_\infty = \frac{1}{1 + \exp\,(\frac{V + 78.8}{8.4})}$$

$$\tau_b = \frac{1}{q10 * 0.0368 * \frac{1}{\exp\left(\frac{v + 111.33209}{12.8433}\right) + 1} + q10 * 0.0345 * \frac{1}{\exp\,(\frac{v + 49.9537}{-49.9537})}}$$

where $q10 = 3^{(T-25.5)/10}$, for temperature T

The M-type potassium channel (Kv7.x): The KM model was adapted from D'Angelo *et al*. (2001), and the current flowing through this potassium channel was:

$$I = gn(V - E_k)$$

The activation gating particle was defined by the following equations:

$$n_{\infty} = \frac{1}{1 + \exp\,(-\frac{\mathrm{v} + 35}{6})}$$

$$\tau_n = \frac{1}{q10 * 0.0033 * \exp\left(\frac{v + 30}{40}\right) + q10 * 0.0033 * \exp\,(\frac{v + 30}{-20})}$$

where $q10 = 3^{(T-22)/10}$, for temperature T

The IK potassium channel (Kca3.1): The middle conductance calcium dependent potassium channel model was adapted from Rubin *et al*. (2006), and the current flowing through this potassium channel was:

$$I = gy(V - E_k)$$

The activation gating particle was defined by the following equations:

$$\alpha_y = \exp\,(\frac{(v + 70)}{27})$$

$$\beta_y = 500 * \frac{0.015\ - [Ca_i]}{\exp\left(\frac{0.015 - [Ca_i]}{0.0013}\right) - 1}, \qquad if\ [Ca_i] < 0.01\, mM$$

$$= 500 * \frac{0.005}{\exp\left(\frac{0.005}{0.0013}\right) - 1}, \qquad otherwise$$

$$y_{\infty} = \frac{\alpha_y * \beta_y}{\alpha_y * \beta_y + 0.05} * qt$$

$$\tau_y = \frac{1}{\alpha_y * \beta_y + 0.05}$$

where $qt = 3^{(T-37)/10}$, for temperature T

The hyperpolarization-activated cyclic-nucleotide-gated 1 channel: The HCN1 channel model was adapted from Solinas *et al*. (2007a and 2007b) and the current flowing through this nonspecific cationic channel was:

$$I = g * (ms + mf)(V - E_h)$$

Where ms and mf represent the gating variables for the slow and fast components of the current through HCN channels, respectively. The activation gating particles for the slow and fast HCN components followed the equations below:

$$mf_{\infty} = (0.002096 * V + 0.97596) * \frac{1}{1 + \exp\left((V + 72.49) * 0.11305\right)}$$

$$ms_{\infty} = (1 - (0.002096 * V + 0.97596)) * \frac{1}{1 + \exp\left((V + 72.49) * 0.11305\right)}$$

$$\tau_{mf} = \frac{\exp\left(\left((0.01371 * V) + 3.368\right) * 2.302585092\right)}{q10}$$

$$\tau_{ms} = \frac{\exp\left(\left((0.01451 * V) + 4.056\right) * 2.302585092\right)}{q10}$$

where $qt = 3^{(T-23)/10}$, for temperature T

The hyperpolarization-activated cyclic-nucleotide-gated 2 channel: The HCN2 channel model was adapted from Solinas *et al*. (2007a and 2007b) and the current flowing through this nonspecific cationic channel was:

$$I = g * (ns + nf)(V - E_h)$$

Where ms and mf represent the gating variables for the slow and fast components of the current through HCN channels, respectively. The activation gating particles for the slow and fast HCN components were described by the following equations:

$$\begin{aligned} r &= 0, \quad if\ V \geq -64.70 \\ &= 1, \quad if\ V \leq -108.70 \\ &= (-0.0227 * V) + (-1.4694)\,, \quad otherwise \end{aligned}$$

$$nf_{\infty} = r * \frac{1}{1 + \exp\left((V + 81.95) * 0.1661\right)}$$

$$ns_{\infty} = (1 - r) * \frac{1}{1 + \exp\left((V + 81.95) * 0.1661\right)}$$

$$\tau_{nf} = \frac{\exp\left(\left((0.0269 * V) + 5.6111\right) * 2.3026\right)}{q10}$$

$$\tau_{ns} = \frac{\exp\Big(\big((0.0152 * V) + 5.2944\big) * 2.3026\Big)}{q10}$$

where $qt = 3^{(T-23)/10}$, for temperature T

The low-voltage-activated calcium channel (Cav3.1): The T-type calcium channel model was adjusted using electrophysiological data from Anwar *et al*. (2012). The current through this channel adhered to GHK conventions, with the default extracellular and cytosolic calcium concentrations set at 2 mM and 5e-05 mM, respectively. The conductance evolution of this channel was described as follows:

$$g(t) = \bar{g}m^2h$$

where m and h, represented the voltage-dependent activation and inactivation gating particles, respectively. The following equations govern their evolution:

$$m_\infty = \frac{1}{1 + \exp\,(\frac{V + 52}{-5})}$$

$$\tau_m = 1, \qquad if\ v < -90,$$

$$= \frac{1 + \frac{1}{\exp\left(\frac{v+40}{9}\right) + \exp\left(\frac{v+102}{-18}\right)}}{qt}, \qquad otherwise$$

$$h_\infty = \frac{1}{1 + \exp\,(\frac{V + 72}{7})}$$

$$\tau_h = \frac{15 + \frac{1}{\exp\left(\frac{v + 32}{7}\right)}}{qt}$$

where $qt = 3^{(T-37)/10}$, for temperature T

The medium-voltage-activated calcium channel (Cav2.3): The R-type calcium channel model was adjusted using electrophysiological data from Sterratt *et al*. (2012). The current through this channel adhered to GHK conventions, with the default extracellular and cytosolic calcium concentrations set at 2 mM and 5e-05 mM, respectively. The conductance evolution of this channel was described as follows:

$$g(t) = \bar{g}m^3h$$

where m and h, represented the voltage-dependent activation and inactivation gating particles, respectively. The following equations govern their evolution:

$$m_\infty = \frac{1}{1 + \exp\left(\frac{V + 48.5}{-3}\right)}$$

$$\tau_m = 50$$

$$h_\infty = \frac{1}{1 + \exp\left(\frac{V + 53}{1}\right)}$$

$$\tau_h = 5$$

The high-voltage-activated calcium channel (Cav2.2): The N-type calcium channel model was adjusted using electrophysiological data from D'Angelo *et al*. (2001). The current through this channel followed GHK conventions, with the default extracellular and cytosolic calcium concentrations set at 2 mM and 5e-05 mM, respectively. The conductance evolution of this channel was described as follows:

$$g(t) = \bar{g}s^2u$$

where s and u, represented the voltage-dependent activation and inactivation gating particles, respectively. The following equations govern their evolution:

$$\alpha_s = q10 * 0.04944 * exp\left(\frac{V + 29.06}{15.87301587302}\right)$$

$$\beta_s = q10 * 0.08298 * exp\left(\frac{V + 18.66}{-25.641}\right)$$

$$\alpha_u = q10 * 0.0013 * exp\left(\frac{V + 48}{-18.183}\right)$$

$$\beta_u = q10 * 0.0013 * exp\left(\frac{V + 48}{83.33}\right)$$

$$s_\infty = \frac{\alpha_s}{\alpha_s + \beta_s}$$

$$\tau_s = \frac{1}{\alpha_s + \beta_s}$$

$$u_\infty = \frac{\alpha_u}{\alpha_u + \beta_u}$$

$$\tau_u = \frac{1}{\alpha_u + \beta_u}$$

where $qt = 3^{(T-20)/10}$, for temperature T

Markovian model: There are certain limitations to HH models. It assumes that the channel is either in open or closed state and the gating variables are independent of each other. Certain lines of evidence show that for inactivating channels the inactivation is not completely independent of activation (Armstrong and Bezanilla, 1977; Bezanilla and Armstrong, 1977; Aldrich *et al.*, 1983). The ion channels can reside in multiple states having a non-zero positive conductivity to the ions at more than one state. Under such cases the multi-state Markovian models are very useful. The assumptions of Markovian models are as follows:

1. The channels are always present in one of the distinct number of states and their entering or exiting a state depends on their respective rate constants.

2. The system is memoryless i.e., the rate of transition from one state to another is independent of the state the system is in.

3. Individual transitions are first order transitions.

For a channel x which conducts at n different states the current through the channel is given as:

$$I_x = \bar{g}_x(O_1 + O_2 + \cdots + O_n)(V - E_x)$$

Therefore, the Markovian model is useful as it accounts for different conformational states and multiple time constants showed by the ion channel under experimental conditions (Armstrong and Bezanilla, 1977; Bezanilla and Armstrong, 1977; Varghese and Boland, 2002; Fink and Noble, 2009). However, it is very difficult to determine the free parameters of the model and certain experimental lines of evidence suggest that the ion channels do not hold the memoryless property.

The sodium resurgent channel, big-conductance calcium-dependent potassium channel, small-conductance calcium-dependent potassium channel and calcium dynamics are modelled using multiple states as Markovian models.

2.3 Intrinsic Measurements for Single Cell Model

Models were validated against an array of 14 characteristic electrophysiological measurements (sub-threshold and supra-threshold) from cerebellar Golgi cells (**Table 2.1**). These measurements are computed as follows: Spontaneous firing frequency (f_0) is computed as total number of spikes during simulation time of 1.5 s divided by the time of simulation. Firing frequency is also calculated for depolarising current injection of 0.2, 0.4 and 0.6 nA. It is calculated as number of spikes during current injection of 1 s after stabilization of 0.5 s.

Action potential (AP) threshold is calculated as the voltage value where dV/dt of the first AP during spontaneous firing crosses 5 V/s. AP peak is the highest voltage value during the time interval of first AP. AP amplitude is the difference between AP peak and AP threshold for the first AP. AP half-width is computed as the time difference between the voltage values at 50% of AP amplitude during depolarisation and repolarisation phase of first AP during spontaneous firing. AP depolarisation, t_{10-90}, is calculated as the time difference between voltages at 10% and 90% of AP during depolarisation phase. Mean subthreshold values, V_m, is calculated as the average of voltage values less than or equal to AP threshold from 10.5 s of voltage trace during spontaneous firing. Spike frequency adaptation for current injection of 0.1 nA and is calculated as $1 - \frac{f_{1s}}{f_{in}}$, where f_{1s} is firing frequency at the end of current stimulus and f_{in} is firing frequency at the start of current stimulus.

We also calculated sag ratio and input resistance for hyperpolarising current injection of 0.3 nA for 1 s after a stabilization period of 0.5 s. Sag ratio is computed as the difference between V_{min} and V_{ss} , where V_{min} is the lowest voltage value during hyperpolarising current injection and V_{ss} is steady-state voltage value calculated as the average of voltage values during the last 5 ms of current injection (from 1495 to 1500 ms). Input resistance (R_{in}) is calculated as $\frac{V_{ss} - V_{rmp}}{0.3}$, where V_{rmp} is average of voltage values 5 ms before the current injection (from 495 to 500 ms). Electrophysiological ranges of the above-mentioned measurements are taken from Forti *et al*., (2006) and is provided in Table 2.1.

Table 2.1: Intrinsic measurements of cerebellar Golgi cells and their respective electrophysiological bounds

These measurements are taken from Forti et al. for *in vitro* GoCs in the presence of synaptic blockers. The ranges given here accounts for a large proportion of variability in the measured data and is calculated using mean, SEM and sample size reported in Forti et al.

	Measurement (unit)	**Symbol**	**Lower bound**	**Upper bound**
1.	Spontaneous firing frequency (Hz)	f_0	1	10
2.	Firing frequency for $\mathrm{I}_{\mathrm{inj}}$ = 0.2nA (Hz)	f_{200}	32	59
3.	Firing frequency for $\mathrm{I}_{\mathrm{inj}}$ = 0.4nA (Hz)	f_{400}	55	90
4.	Firing frequency for $\mathrm{I}_{\mathrm{inj}}$ = 0.6nA (Hz)	f_{600}	76	119
5.	AP threshold (mV)	$\mathrm{AP}_{\mathrm{thres}}$	-60	-50
6.	AP peak (mV)	$\mathrm{AP}_{\mathrm{peak}}$	15	1000
7.	AP amplitude (mV)	$\mathrm{AP}_{\mathrm{amp}}$	70	2000
8.	AP trough (mV)	$\mathrm{AP}_{\mathrm{trough}}$	-83	-67
9.	AP half width (ms)	APHW	0.8	2
10.	AP depolarisation (µs)	t_{10-90}	230	650
11.	Mean V_{m} subthreshold (mV)	$\mathrm{V}_{\mathrm{m\ sub}}$	-76	-60
12.	Spike frequency adaptation of $\mathrm{I}_{\mathrm{inj}}$ = 0.1nA	SFA_{100}	0	0.34
13.	Input resistance (MΩ)	R_{in}	65	320
14.	Sag ratio (mV)	Sag	1	22

2.4 Hand Tuning

Each GoC model consists of 5 different compartments. Each of these compartments have differential expression of ion channels (**Table 2.2**). Conductance of the thirteen ion channels in different compartments with axial resistance, reversal potential and leak conductance compose parameter space of a GoC model. Each GoC model has 40 parameters. At first, a GoC model is initiated with random parameter values and its intrinsic measurements are calculated. Parameter values are changed so that measurements fall into the experimental range. This process gave an idea about the sensitivity of a given parameter and properties of different ion channels used. The model where most of the measurements fall into the experimental range is called the base model. Parameters of the base model is used to come up with valid models.

Table 2.2: Parameters, their values in the base model and range for generating random models

The parameter ranges are chosen to be around base value where for most of the cases the range is calculated as 0.5-2 times the value of the base model.

	Parameter (unit)	Symbol	Base value	Range
Soma				
1.	Axial resistance (Ωcm)	soma Ra	122	100-300
2.	Reversal potential (mV)	soma epas	-55	-70 - -55
3.	Leak conductance(S/cm^2)	soma gpas	0.0003	0.000015 - 0.00006
4.	Resurgent sodium conductance(S/cm^2)	soma $\mathrm{Na_V}$1.6	0.03189	0.015945 - 0.06378
5.	KDR conductance(S/cm^2)	soma $\mathrm{K_V}$1.1	7.21e-05	3.61e-05 - 1.44e-04
6.	Inactivating KDR conductance(S/cm^2)	soma $\mathrm{K_V}$3.4	0.089	0.0445 - 0.178
7.	A-type potassium conductance(S/cm^2)	soma $\mathrm{K_V}$4.3	0.00083029	0.000415145 - 0.00166058
8.	BK conductance(S/cm^2)	soma $\mathrm{K_{Ca}}$1.1	0.0046044	0.0023022 - 0.0092088
9.	IK conductance(S/cm^2)	soma $\mathrm{K_{Ca}}$3.1	0.054535	0.0272675 - 0.10907
10.	N-type calcium conductance(S/cm^2)	soma $\mathrm{Ca_V}$2.2	0.036212	0.018106 - 0.072424
11.	T-type calcium conductance(S/cm^2)	soma $\mathrm{Ca_V}$3.1	3.12e-05	1.56e-05 - 6.24e-05
Axonal initial segment				
12.	Axial resistance (Ωcm)	AIS Ra	122	100-300
13.	Reversal potential (mV)	AIS epas	-55	-70 - -55
14.	Leak conductance(S/cm^2)	AIS gpas	0.00003	0.000015 - 0.00006
15.	HCN1 conductance(S/cm^2)	AIS HCN1	0.011734	0.005867 - 0.023468
16.	HCN2 conductance(S/cm^2)	AIS HCN2	0.0020148	0.0010074 - 0.0040296
17.	Resurgent sodium conductance(S/cm^2)	AIS $\mathrm{Na_V}$1.6	0.027572	0.013786 - 0.055144
18.	M-type potassium conductance(S/cm^2)	AIS $\mathrm{K_V}$7.x	0.00016356	0.00008178 - 0.00032712
19.	BK conductance(S/cm^2)	AIS $\mathrm{K_{Ca}}$1.1	0.19126	0.09563 - 0.38252
20.	N-type calcium conductance(S/cm^2)	AIS $\mathrm{Ca_V}$2.2	0.043983	0.0219915 - 0.087966

Apical dendrites				
21.	Axial resistance (Ωcm)	adend Ra	122	100-300
22.	Reversal potential (mV)	adend epas	-55	-70 - -55
23.	Leak conductance(S/cm^2)	adend gpas	0.00003	0.000015 - 0.00006
24.	Resurgent sodium conductance(S/cm^2)	adend Na$_V$1.6	0.012912	0.006456 - 0.025824
25.	BK conductance(S/cm^2)	adend K$_{Ca}$1.1	0.010592	0.005296 - 0.021184
26.	SK conductance(S/cm^2)	adend K$_{Ca}$2.2	0.0010344	0.0005172 - 0.0020688
27.	R-type calcium conductance(S/cm^2)	adend Ca$_V$2.3	0.00087085	0.000435425 - 0.0017417
28.	T-type calcium conductance(S/cm^2)	adend Ca$_V$3.1	2.21e-05	1.10e-05 - 4.41e-05
Basal dendrites				
29.	Axial resistance (Ωcm)	bdend Ra	122	100-300
30.	Reversal potential (mV)	bdend epas	-55	-70 - -55
31.	Leak conductance(S/cm^2)	bdend gpas	0.00003	0.000015 - 0.00006
32.	Resurgent sodium conductance(S/cm^2)	bdend Na$_V$1.6	0.04245	0.021225 - 0.0849
33.	BK conductance(S/cm^2)	bdend K$_{Ca}$1.1	0.018213	0.0091065 - 0.036426
34.	SK conductance(S/cm^2)	bdend K$_{Ca}$2.2	0.0015	0.00075 - 0.003
35.	N-type calcium conductance(S/cm^2)	bdend Ca$_V$2.2	0.0021606	0.0010803 - 0.0043212
Axon				
36.	Axial resistance (Ωcm)	Axon Ra	122	100-300
37.	Reversal potential (mV)	axon epas	-55	-70 - -55
38.	Leak conductance(S/cm^2)	axon gpas	0.000001	0.0000005 - 0.000002
39.	Resurgent sodium conductance(S/cm^2)	axon Na$_V$1.6	0.054978	0.027489 - 0.109956
40.	Inactivating KDR conductance(S/cm^2)	axon K$_V$3.4	0.0046678	0.0023339 - 0.0093356

2.5 Multi-Objective Multi-Parametric Stochastic Search

The inherent variability in parameters and measurements observed in biological neurons necessitates the evaluation of neuronal physiology using a diverse set of models, rather than relying on a single model that has been manually adjusted (Prinz *et al.*, 2003; Marder and Taylor, 2011; Rathour and Narayanan, 2019; Sinha and Narayanan, 2022). In order to investigate whether the expression of all 14 intrinsic measurements in a population of cerebellar GoCs is degenerate in terms of the ion channel combinations that can produce them, we employed a multi-parametric, multi-objective stochastic search (MPMOSS) algorithm (Foster *et al.*, 1993; Goldman *et al.*, 2001; Prinz *et al.*, 2003; Marder and Taylor, 2011; Rathour and Narayanan, 2012, 2014; Anirudhan and Narayanan, 2015; Srikanth and Narayanan, 2015; Mukunda and Narayanan, 2017). This stochastic search involved 40 parameters and was validated against 14 sub- and supra-threshold measurements in order to match in vitro electrophysiological recordings from GoCs. To execute the MPMOSS algorithm, we defined a model neuron by assigning specific values to each of the 40 parameters, which were randomly selected from a uniform distribution defined by the parameter values of the base model. For each randomly constructed model, which ensured that the parametric ranges are not biased with any constraints, we computed all 14 intrinsic measurements and compared them to their respective electrophysiological bounds. A model that met all 14 validation criteria was considered valid (**Figure 2.2**). We repeated this process for 50,000 randomly chosen sets of parameters and validated these models against the 14 measurements. Since each of these 50,000 picks was independent and random, each model had unique values for all 40 parameters. This randomization process ensured that individual parameters were not discretized and limited to specific values, and that there were no constraints on the relationships between different parameters.

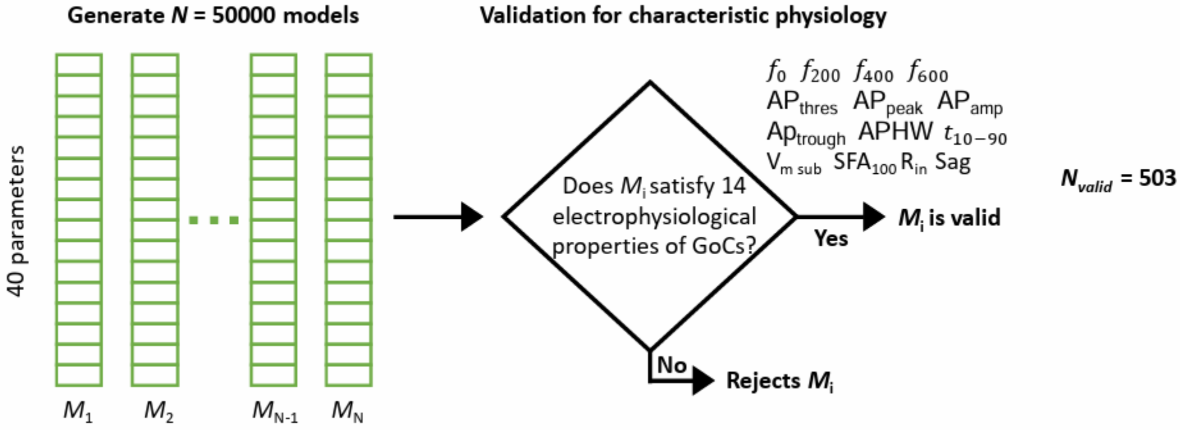

Figure 2.2: Illustration of MPMOSS algorithm spanning 40 search parameters (Table 2.2) and 14 validation measurements (Table 2.1).

2.6 Gap Junctions

Class ParallelContext of NEURON in HOC was used to connect two cells with gap junctions (GJ). This enables parallel simulation of models incorporating GJs and/or synapses wherein the postsynaptic conductance dynamically relies on the presynaptic voltage. The gap junction is like a compartment where current reduces according to the its resistance. It is bidirectional in nature i.e, it allows current flow from cell 1 to cell 2 as well as from cell 2 to cell 1. Also, it is possible to rectify the GJ, i.e., resistance to the flow in one direction (cell 1 to cell 2) can be different than resistance to the flow in the opposite direction (cell 2 to cell 1).

Two GoCs, cell 1 and cell 2, were connected with GJs. GJs were placed either between somas (at 0.5 of the normalized length), between apical dendrites (at 0.9 of the normalized length) or between basal dendrites (at 0.9 of the normalized length). Default GJ was bidirectional with resistance of 0.9 nS from either side. Current is injected into the soma of cell 1 and voltage is recorded from the soma of both the cells (**Figure 2.3**).

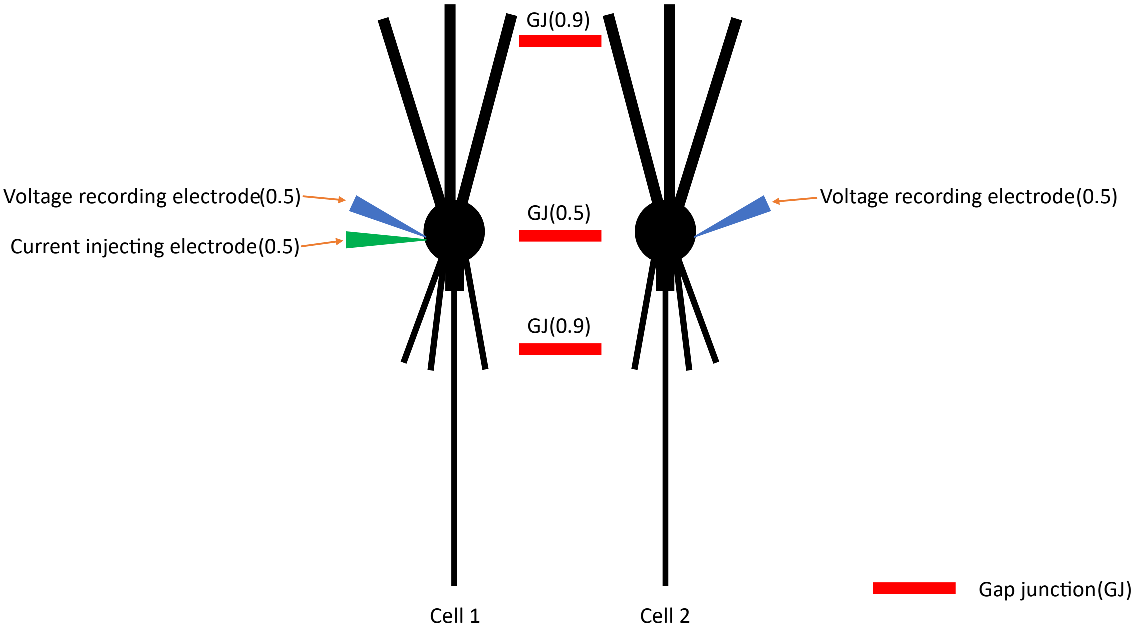

Figure 2.3: Illustration of two cell-network setup: placement of GJs, current injecting and voltage recording electrode in the analyses of two-cell network.

2.7 Two-Cell Network Characterisation

To characterize the two cell-network we connected two identical GoCs at soma, or at apical dendrites or at basal dendrites. We calculated the following measurements:

Impedance: To obtain the impedance-based measurements, voltage response to a chirp current stimulus was recorded. The chirp stimulus was injected into cell 1 and the voltage response was recorded from both cell 1 and cell 2. To ensure the cells do not fire during injection of chirp stimulus the signal is negatively shifted by 200 pA. The signal is given 5s after the start of the simulation to let the system stabilize and during this time the spontaneous firing is supressed by injecting hyperpolarising current injection of 200 pA. The chirp stimulus used here was a constant-amplitude (50 pA peak-to-peak) sinusoidal current, with frequency increasing linearly from 0 to 25 Hz over a period of 25s (Narayanan and Johnston, 2007, 2008; Hemond *et al.*, 2009; Basak and Narayanan, 2018). The Fourier transform of the voltage response from cell 1 and cell 2 was divided by the Fourier transform of the chirp current to obtain complex local impedance $[|Z_l(f)|]$ and complex transfer impedance$[|Z_t(f)|]$, respectively, as a function of frequency (f). Impedance amplitude profile $[|Z(f)|]$ was calculated as follows:

$$|Z(f)| = \sqrt{Re[Z(f)]^2 + Im[Z(f)]^2}$$

Where $Re[Z(f)]^2$ and $Im[Z(f)]^2$ are the real and imaginary parts of the impedance $[|Z(f)|]$, respectively. The resonance frequency was defined as the frequency at which the value of $|Z(f)|$ reached its maximum $(|Z|_{max})$.

Gain: Gain is calculated as the ratio of steady-state voltage response of cell 2 and steady-state voltage response of cell 1 for a current injection of -0.3 nA into cell 1. Steady-state voltage response is computed as average of voltage trace of last 5 ms of the simulation. Gain was measured as a function of GJ conductance and GJ location where range of conductance used is from 0.5 nS to 2.5 nS with an increment of 0.1 nS and range of location used is from 0 to 1 with an increment of 0.1 in normalized lengths.

Resynchronization after current perturbation: To compare the resynchronization time after current perturbation for different location of GJ, 0.2 nA and -0.3 nA of current was injected into cell 1 for 1 s and the simulation was allowed to run for 30 s. Time difference between consecutive spikes in cell 1 and cell 2 was plotted as the function of spike number after current injection to visualize the time delay after which two cells synchronize.

2.8 Computational details

All simulations were conducted using the NEURON programming environment (Carnevale and Hines, 2006) at 25°C. The simulation step size was set as 25 μs except for scripts used to calculate suprathreshold measurements (AP peak, AP trough, AP threshold, AP amplitude, AP half-width and AP depolarisation) for which step size was 10 μs to increase temporal resolution. Data analysis and graph plotting were performed using custom-written MATLAB scripts. All data points from all simulations and models were reported and depicted as bee swarm or scatter plots to prevent any misleading interpretations arising solely from reporting summary statistics (Marder and Taylor, 2011; Rathour and Narayanan, 2014).

Chapter 3: Results

We built a biophysically and morphologically realistic base model of a cerebellar GoC neuron, endowed with characteristic active and passive properties adapted from earlier studies. The base model satisfied several signature electrophysiological characteristics of cerebellar GoC neuron.

3.1 Multi-parametric, multi-objective stochastic search yielded a heterogeneous population of cerebellar GoC neuron models showing characteristic physiology

The inclusion of just one hand-tuned model when conducting analyses and evaluations results in the introduction of biases into the overall conclusions. An alternative approach would be to construct a population of models, all of which possess the characteristic physiological features of the system being studied (Prinz *et al.*, 2003; Marder and Taylor, 2011), and to examine the phenomena of interest within this population. In addition to avoiding the inherent biases and disadvantages associated with utilizing a single model for all analyses, this population of models also allows for the assessment of heterogeneities and degeneracy within the system (Prinz *et al.*, 2004; Rathour and Narayanan, 2014, 2019; Anirudhan and Narayanan, 2015; Srikanth and Narayanan, 2015; Mukunda and Narayanan, 2017; Basak and Narayanan, 2018, 2020; Mittal and Narayanan, 2018; Mishra and Narayanan, 2019; Jain and Narayanan, 2020; Seenivasan and Narayanan, 2020; Goaillard and Marder, 2021; Roy and Narayanan, 2021; Shridhar *et al.*, 2022). In order to generate this population of models, a MPMOSS algorithm was employed, which involved 40 parameters (**Table 2.2**) and 14 different objectives (**Table 2.1**). A total of 50,000 distinct models were randomly generated, and from this pool, a small subset of 503 models (approximately 1.006%) were identified as satisfying all validation criteria pertaining to the characteristic features of cerebellar GoC neurons (Forti *et al.*, 2006). The 14 electrophysiological measurements were plotted for this model population in order to determine if they clustered around their respective base model values or if they exhibited a distribution that spanned the range of valid model measurements. If the measurements were clustered, this would suggest a near-homogeneous population of models, whereas a distribution spanning the range of in vitro electrophysiological counterparts would indicate a heterogeneous model population that reflects the experimental variability observed in the measurements. It was found that all measurements spanned a large range, with the majority covering the entire min-max range of their respective bounds (**Figure 3.1**). Thus, these 503 valid models exhibited pronounced heterogeneities in their physiological properties, which accurately reflected the heterogeneities observed in cerebellar GoC neurons.

A few models which had spontaneous firing frequency of less than 4 Hz went silent after initial few spikes. Out of 503 valid models, there were 17 such models. We rejected them to get 486 valid models that satisfied the validation criteria of cerebellar GoC neurons. Although 14 distinct measurements were utilized for the purpose of validation, it was imperative to verify that these measurements were truly assessing various aspects of cerebellar GoC neuron physiology. The presence of strong correlations between these measurements would suggest that the validation process did not entail independent measurements, but rather confirmed the same attribute via dissimilar measurements. Furthermore, if there were strong correlations across multiple measurements, it would imply that certain measurements heavily relied on the expression and properties of a specific channel. To evaluate this, we calculated Pearson's correlation coefficient among all physiological measurements across valid models. The majority of these measurements displayed weak correlations, with only a small number of pairs exhibiting strong correlations (**Figure 3.2**). Notably, measurements that demonstrated strong correlations were those that were known to depend critically on specific ion channels. For example, there were strong correlations between the two suprathreshold excitability measures (f_{200} and f_{200}) as well as between AP amplitude and AP peak. This is expected as the suprathreshold excitability measures are influenced by the same parameters. Interestingly, f_0 did not display any correlation with the other measurements.

In conclusion, while a minority of measurements exhibited strong pairwise correlations, the majority of these correlations were weak, further highlighting the absence of one-to-one relationships between channels and measurements.

3.2 Cellular-scale degeneracy in the manifestation of characteristic physiological properties of cerebellar GoC neuronal models

To evaluate whether specific parametric values are necessary for the emergence of characteristic physiological properties in a population of cerebellar granule cell (GoC) neuronal models, or if disparate parametric combinations across the parametric space

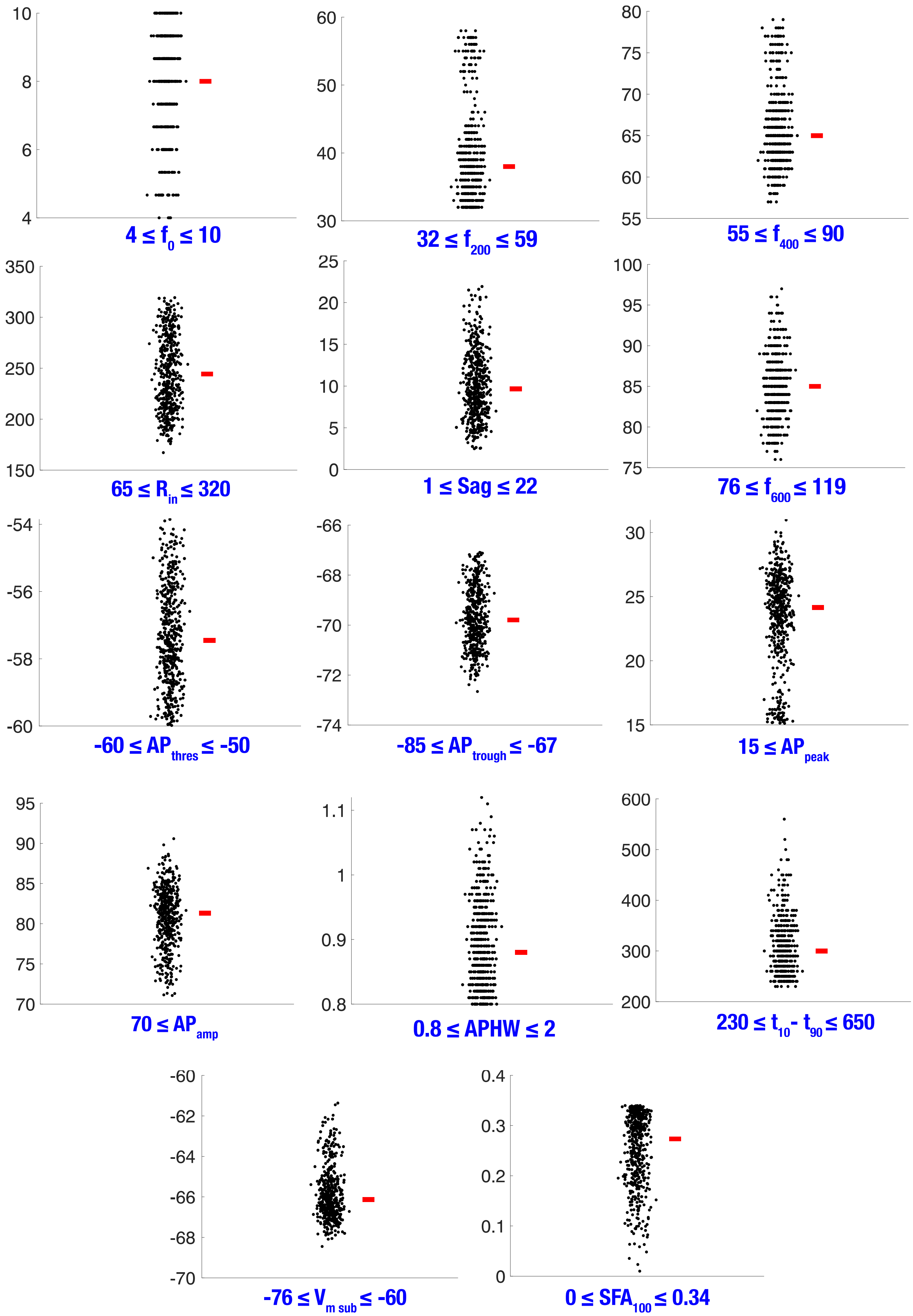

Figure 3.1: Bee-swarm plots of 14 measurements. All the valid models generated show a heterogeneous distribution of measurements in the physiological bound characteristic of a GoC. The red bars on the right-hand side of each plot shows the median of the distribution.

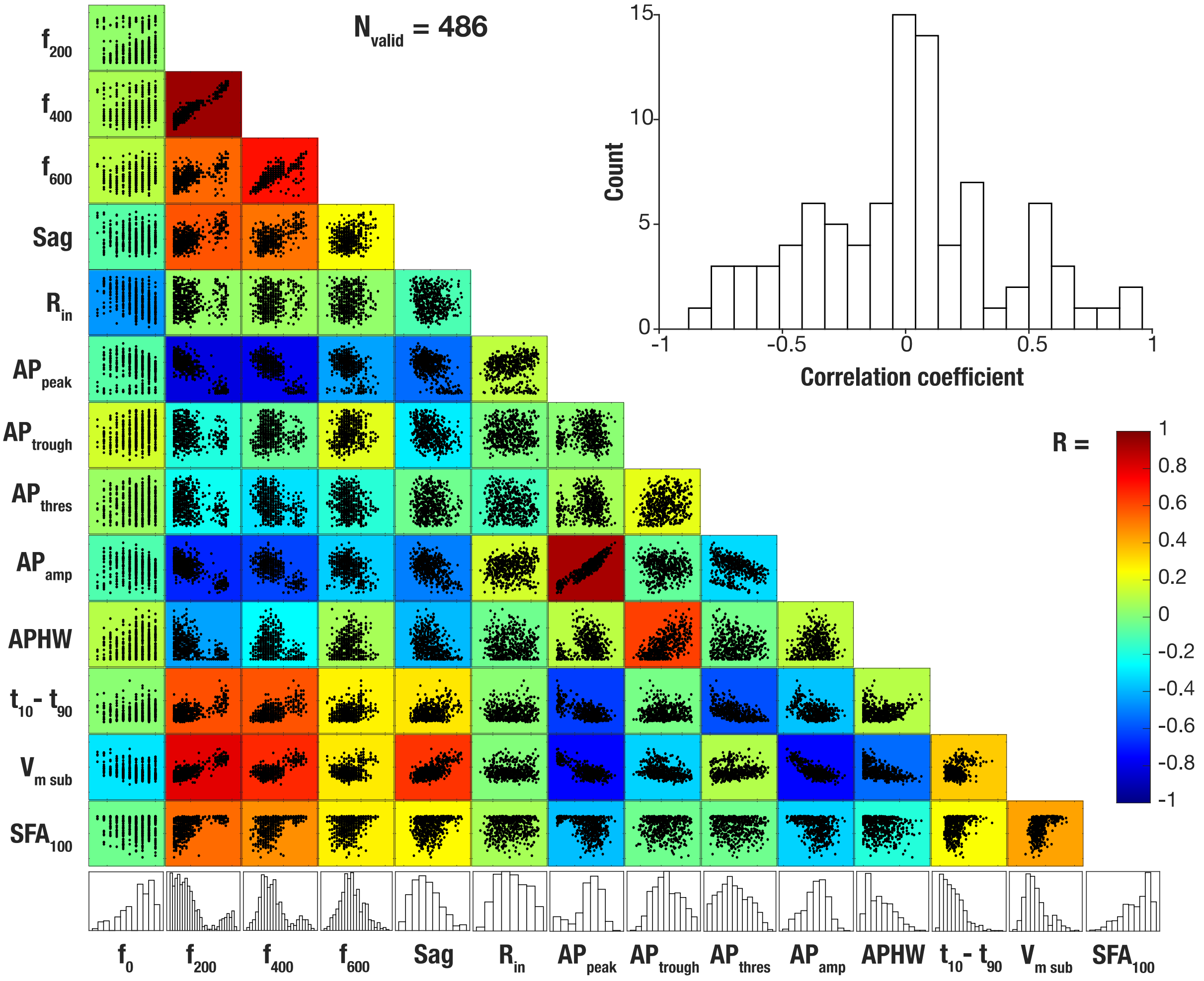

Figure 3.2: Pairwise correlations between 14 measurements for 486 valid models. Each scatter plot depicts correlation values between two given measurements for all 486 valid models. The scatter plot data is overlaid on a heat map that shows correlation coefficient for a given measurement pair. Negatively correlated measurement pairs are associated with blue colour whereas positively correlated measurement pairs are associated with red colour and the other colours in between are according to the colour bar on the right. The histogram in the last row depicts the spread of each measurement across all valid models. The histogram on the top is for 91 correlation coefficients calculated for each measurement pair.

could enable the manifestation of these signature physiological properties, thus implying degeneracy, we initially selected five random models out of a total of 486 models. These selected models were chosen based on their similarity in physiologically relevant intrinsic measurements (**Figure 3.3A - E**). We then normalized each of the 40 parameters from these five models by referring to their respective minimum and maximum values. Our findings revealed that although the physiological measurements were highly similar and representative of cerebellar GoC neurons, none of the models exhibited a specific trend in their parametric values. Instead, most parameters spanned the entire allowed range (**Figure 3.3F**). These observations provide evidence that disparate parametric combinations can contribute to the manifestation of similar characteristic physiological properties. This ability of disparate parametric combinations to elicit characteristic physiology has also been demonstrated in other types of neurons. Therefore, our results indicate that cerebellar GoC neurons with signature physiological characteristics can be generated using various parametric combinations. The five models selected in this study serve as an illustrative example of degeneracy at the cellular scale.

To investigate whether there were clusters in the distribution of parameters that governed the 486 valid models, we graphed the distributions of the 40 parameters that characterized these neuronal models and observed that they were distributed across their respective bounds (**Figure 3.4**). Furthermore, these parameters did not exhibit strong pairwise correlations, indicating that changes in one parameter were compensated for by multiple different parameters rather than just one. It is worth noting that the range of individual parameters spanning their entire minimum-to-maximum range or the absence of strong pairwise correlations among them does not imply that any combination of these parameters could produce valid cerebellar GoC neuron models. It is essential to emphasize that only 486 out of the 50,000 models were considered valid, suggesting that a large majority of the models (~98.994%) within the same parametric range were rejected due to their failure to satisfy the characteristic physiological properties of cerebellar GoC neurons. Therefore, the lack of structure in the underlying parameters should not be interpreted as evidence that any combination of parameters would yield valid cerebellar GoC neurons. Instead, the absence of structure in the valid parametric space should be interpreted as evidence for the presence of degeneracy, where distinct (yet specific) combinations of parameters result in similar physiological properties (Edelman and Gally, 2001; Prinz *et al.*, 2004; Taylor *et al.*, 2009; Rathour and Narayanan, 2012, 2014, 2019; Anirudhan and Narayanan, 2015; Srikanth and Narayanan, 2015; Rathour *et al.*, 2016; Das *et al.*, 2017; Basak and Narayanan, 2018, 2020; Migliore *et al.*, 2018; Mittal and Narayanan, 2018; Mishra and Narayanan, 2019, 2021; Jain and Narayanan, 2020; Seenivasan and Narayanan, 2020; Goaillard and Marder, 2021; Roy and Narayanan, 2021; Shridhar *et al.*, 2022).

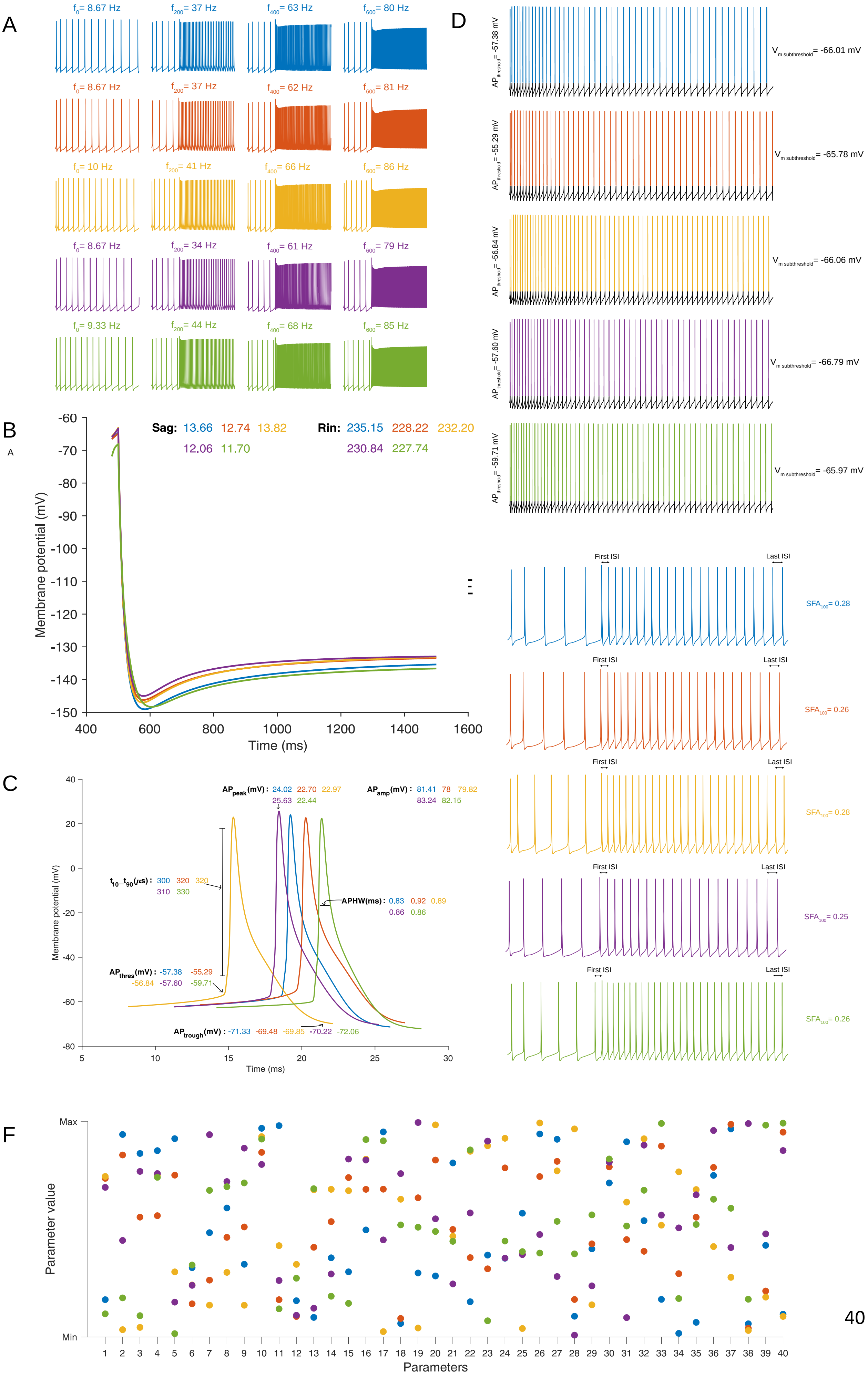
A
f_0= 8.67 Hz
f_{200}= 37 Hz
f_{400}= 63 Hz
f_{600}= 80 Hz
f_0= 8.67 Hz
f_{200}= 37 Hz
f_{400}= 62 Hz
f_{600}= 81 Hz
f_0= 10 Hz
f_{200}= 41 Hz
f_{400}= 66 Hz
f_{600}= 86 Hz
f_0= 8.67 Hz
f_{200}= 34 Hz
f_{400}= 61 Hz
f_{600}= 79 Hz
f_0= 9.33 Hz
f_{200}= 44 Hz
f_{400}= 68 Hz
f_{600}= 85 Hz
B
A
Sag: 13.66 12.74 13.82
12.06 11.70
Rin: 235.15 228.22 232.20
230.84 227.74
Membrane potential (mV)
-60
-70
-80
-90
-100
-110
-120
-130
-140
-150
400
600
800
1000
1200
1400
1600
Time (ms)
C
AP_{peak}(mV): 24.02 22.70 22.97
25.63 22.44
AP_{amp}(mV): 81.41 78 79.82
83.24 82.15
t_{10}–t_{90}(μs): 300 320 320
310 330
APHW(ms): 0.83 0.92 0.89
0.86 0.86
AP_{thres}(mV): -57.38 -55.29
-56.84 -57.60 -59.71
AP_{trough}(mV): -71.33 -69.48 -69.85 -70.22 -72.06
Membrane potential (mV)
40
20
0
-20
-40
-60
-80
5
10
15
20
25
30
Time (ms)
D
$AP_{threshold}$= -57.38 mV
$V_{m\ subthreshold}$= -66.01 mV
$AP_{threshold}$= -55.29 mV
$V_{m\ subthreshold}$= -65.78 mV
$AP_{threshold}$= -56.84 mV
$V_{m\ subthreshold}$= -66.06 mV
$AP_{threshold}$= -57.60 mV
$V_{m\ subthreshold}$= -66.79 mV
$AP_{threshold}$= -59.71 mV
$V_{m\ subthreshold}$= -65.97 mV
First ISI
Last ISI
SFA_{100}= 0.28
First ISI
Last ISI
SFA_{100}= 0.26
First ISI
Last ISI
SFA_{100}= 0.28
First ISI
Last ISI
SFA_{100}= 0.25
First ISI
Last ISI
SFA_{100}= 0.26
F
Max
Min
Parameter value
1
2
3
4
5
6
7
8
9
10
11
12
13
14
15
16
17
18
19
20
21
22
23
24
25
26
27
28
29
30
31
32
33
34
35
36
37
38
39
40
Parameters

Figure 3.3: Emergence of degeneracy in electrophysiological measurements of 5 randomly selected GoC models with very similar measurements. A: voltage traces of 5 models for spontaneous firing and current injections of 200 pA, 400 pA, and 600 pA to calculate firing frequency for different current injections. B: Voltage trace of models for negative current injection of 300 pA to calculate subthreshold measurements. C: Voltage trace of first action potential during spontaneous firing to calculate suprathreshold measurements. D: Voltage trace of 10.5 s to calculate mean subthreshold values. E: Voltage trace to calculate spike frequency adaptation for current injection of 100 pA. F: Plot depicting distribution of normalised parameter values of 5 randomly selected models spanning the respective range as mentioned in Table 2.2. Five colours represent five randomly selected models.

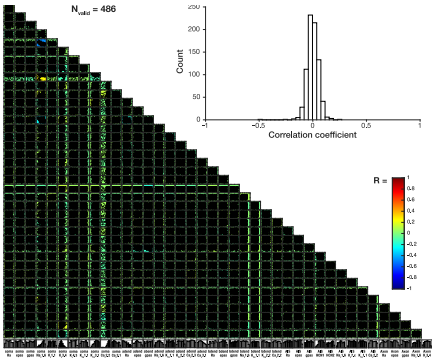

Figure 3.4: Pairwise correlations between 40 parameters for 486 valid models. Each scatter plot depicts correlation values between two given parameters for all 486 valid models. The scatter plot data is overlaid on a heat map that shoes correlation coefficient for a given parameters pair. Colour of the parameter pair and the corresponding correlation coefficient is according to the colour bar on the right. The histogram in the last row depicts the spread of each parameter across all valid models. The histogram on the top is for 780 correlation coefficients calculated for each parameters pair.

3.3 Current perturbation in one cell affects firing frequency of the other cell

To make sure if GoC are indeed connected via GJs and to see the effect of current injection into one cell to the other, we injected constant current amplitude of -0.3 nA, 0.2 nA and 0.4 nA into cell 1. Cell 1 is connected with cell 2 through GJ of conductance 0.9 nS. When no current is injected both the cells fire synchronously (**Figure 3.6A**), but this firing rate is a litter faster (faster by 0.2 ms) than when a single GoC model fires spontaneously (**Figure 3.5**). This increase in firing rate could be because of back-propagation of spike signals from both the cells. Firing of cell 2 is suppressed on current injection of -0.3 nA into cell1, whereas firing rate of cell 2 increases on depolarising current injection into cell1 (**Figure 3.6B**). Increase in firing rate was more for 0.4 nA current injection than for 0.2 nA (**Figure 3.6C and D**). We observe ripples in spike afterhyperpolarisation of cell 2 corresponding to spikes in cell 1 which are responsible for faster depolarisation of membrane potential. These ripples occur more frequently for higher depolarising current injection.

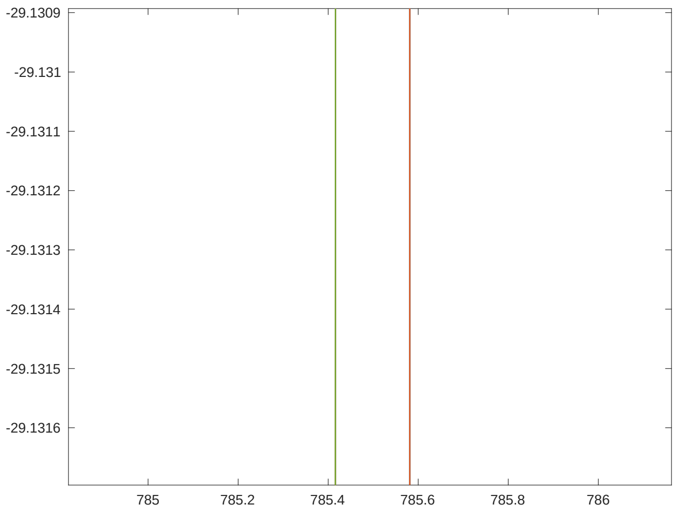

Figure 3.5: Zoomed in voltage trace for spontaneous firing of single cell (red) and two cells connected with GJs (green). X-axis is time in ms and Y axis is voltage values in mV.

3.4 Signals passing through gap junctions undergo low pass filtering and exhibit resonance at low frequency

GoC acts as a low pass filter where it allows for low frequency signal to propagate to the next cell. This is true regardless of the location of the GJ in different compartments (**Figure 3.7A**). Signals passing through GJ also undergo low pass filtering due to the RC property of the membrane. The distance a signal travels in both neurons contributes to its RC filtering. The nature of filtering depends upon the conductance of ion channels expressed in the compartment that are being traversed by the signal. The GJ itself is just a resistor which do not offer any filtering by itself. The transfer of the signal to the next cell also show resonance for low frequency activity. The magnitude of transfer impedance is higher for GJ present at soma than for GJs present in other compartments (**Figure 3.7B**). We observed resonance of 1.76 Hz for GJ present at apical dendrite, 1.88 Hz for GJ present at basal dendrite and 1.68 Hz for GJ present at soma.

3.5 Gain of signal through GJ increases for increase in GJ conductance and decreases for increase in distance of GJ location away from soma

Gain defined as ratio of steady-state voltage of cell 2 and steady-state voltage of cell 1 increases with increase in GJ conductance from 0.5 nS to 2.5 nS. The gain increases

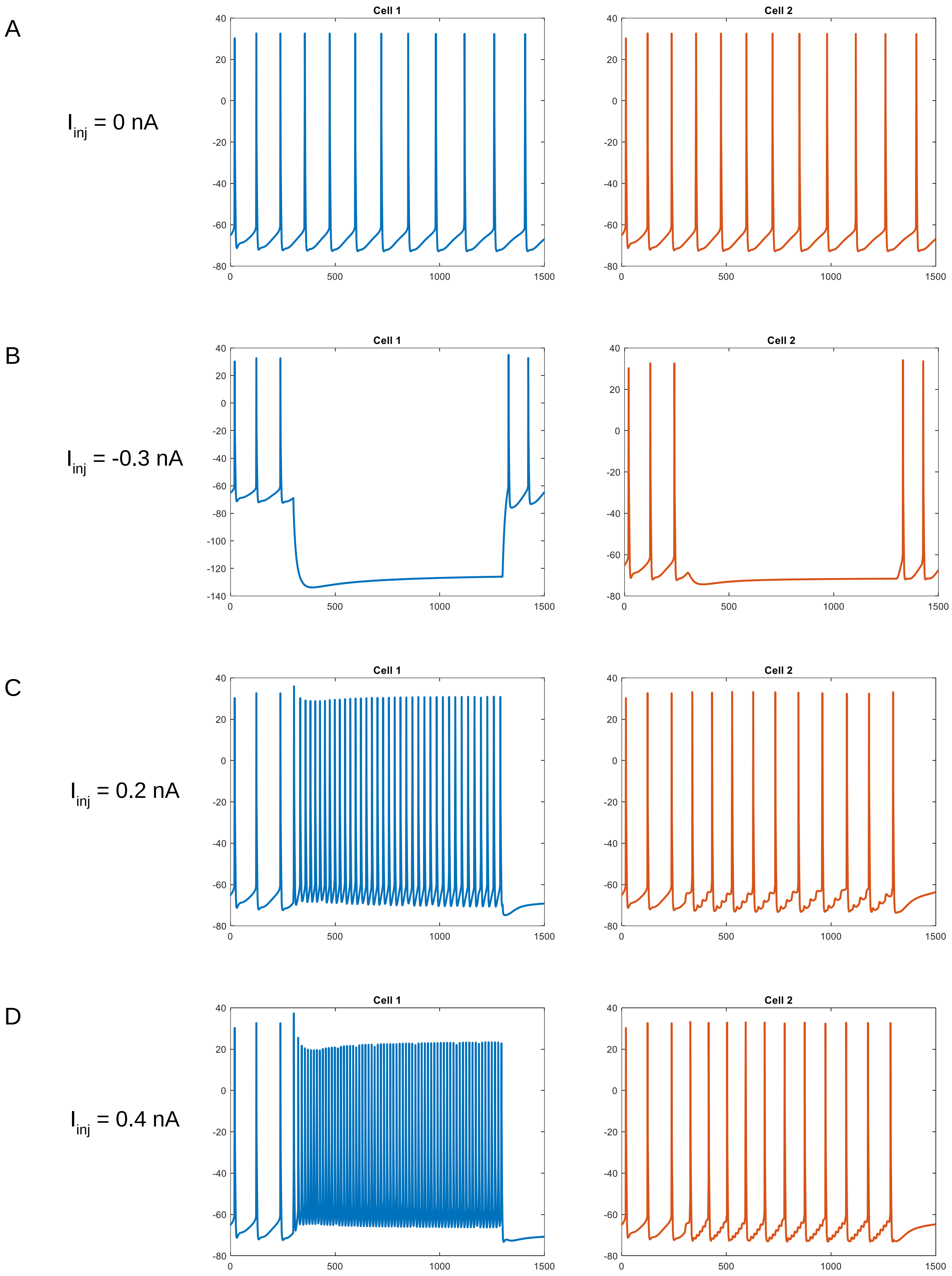

Figure 3.6: Current injection in cell 1 and its effects on cell 2 in a two cell GJ connected network. A, B, C and D are voltage traces of cell 1 and cell 2 for current injection of 0 nA, -0.3 nA, 0.2 nA and 0.4 nA into cell 1 respectively.

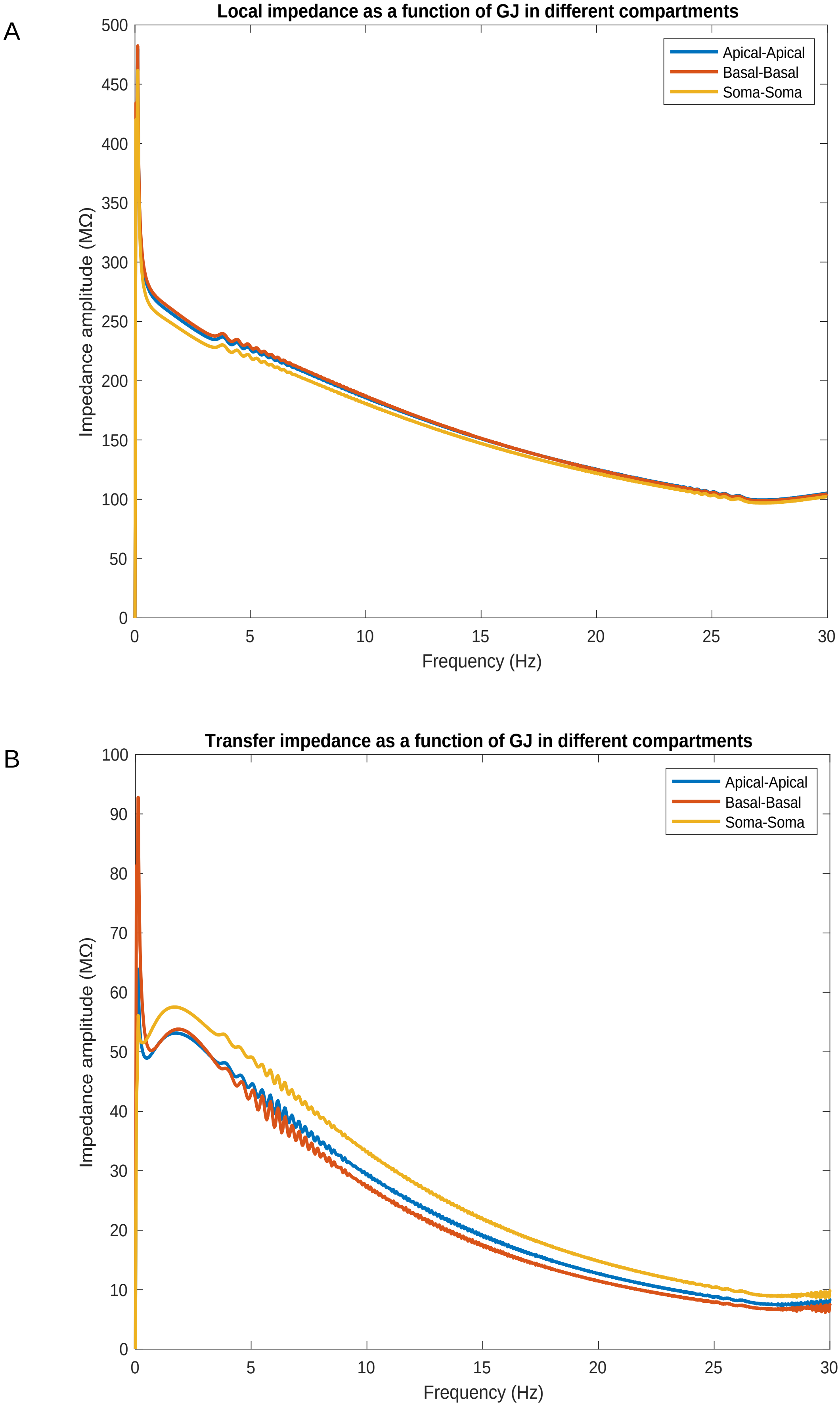

Figure 3.7: A and B are the graphs for local and transfer impedance as a function of GJ in different compartments respectively.

supra linearly for GJs in all the compartments but the increase is highest for GJ in soma and least for GJ in basal dendrite (**Figure 3.8**). Gain is highest for GJ in soma and lowest for GJ in basal dendrite to begin with and this difference amplifies as we increase GJ conductance. This could be because of the difference in the location of GJ where signal travels a longer distance for GJ present in apical and basal dendrites. Interestingly, gain of signal for GJ at apical dendrite is always greater than gain of signal for GJ at basal dendrite even when signal ought to travel longer distance in apical dendrite. This could be attributed to the differences in ion channels in both of the dendrites where apical dendrites have R and T type calcium channels which are low voltage activated and give transient calcium currents whereas basal dendrite have N type calcium channel which are high voltage activated and give long lasting calcium currents. The different calcium currents activate calcium dependent potassium channels differently due to which apical dendrites which are endowed with R and T type calcium channels are better at signal propagation than basal dendrites (I'm not sure about the reason because gain is calculated using hyperpolarising current

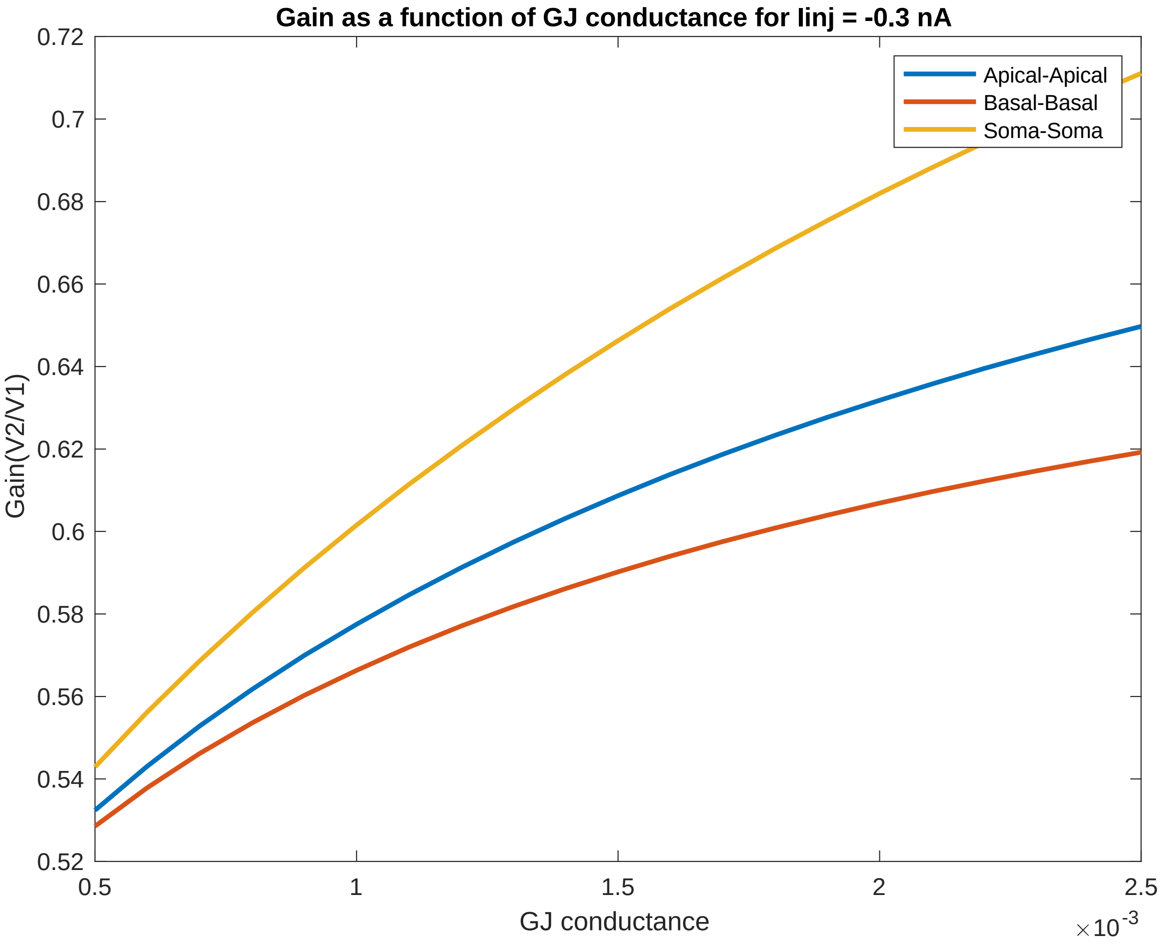

Figure 3.8: Plot for gain as a function of GJ conductance for Iinj = -0.3 pA (for supressing spontaneous firing to calculate gain) in the presence of GJs in different compartments.

injection which gives sag and which is dependent upon h current and not upon calcium or potassium currents).

Gain is also plotted as a function of different location of GJ in the same compartment (**Figure 3.9**). Gain remains almost constant for different locations of GJ in soma, which could be attributed to the small size of soma (20 µm × 10 µm). Gain decreases sub linearly for GJs situated further away from soma in apical and basal dendrites. The gain is calculated in the subthreshold regime thus signal attenuates more for GJs present further away from soma. Gain is same for all the compartments to begin with as then GJs are placed closest to soma. The gain decreases more for basal dendrites than for apical dendrites, which could be because of differential expression of ion channels in these two different dendrites.

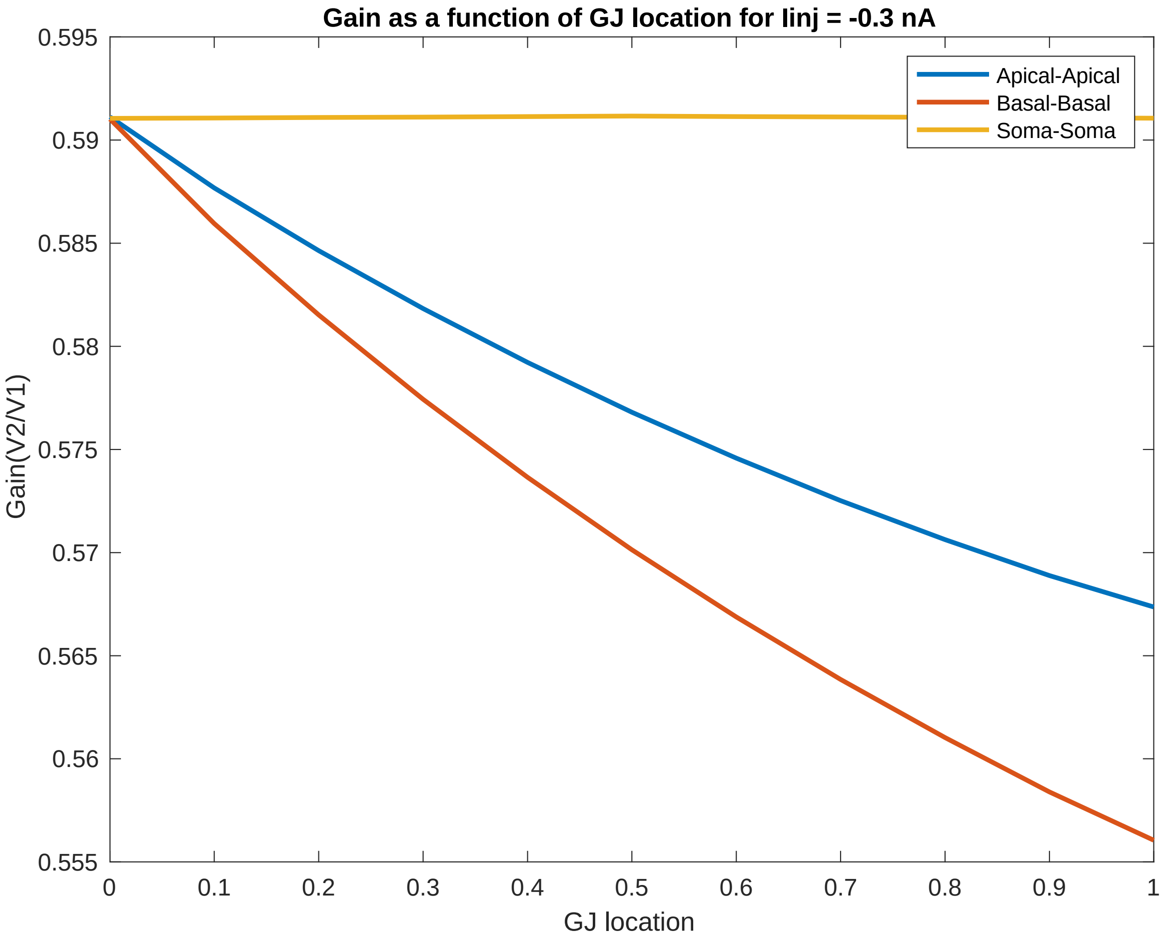

Figure 3.9: Plot for gain as a function of GJ location for Iinj = -0.3 pA (for supressing spontaneous firing to calculate gain) in the presence of GJs in different compartments.

3.6 Two-cell GoC network resynchronizes after current perturbation in one cell

The two cells in the two-cell GoC network fires simultaneously without any external current perturbation. When a depolarising or a hyperpolarising current stimulus is injected into one of the cells, it changes firing pattern of the other cell as well for the duration of current injection and afterwards. After how long does the two cells resynchronize their firing pattern after the end of current perturbation? To answer this, we injected 0.2 nA and -0.3 nA of current into cell 1 and let the simulation run for 30 s to see the trend of resynchronization in time of the two-cell network (**Figure 3.10**).

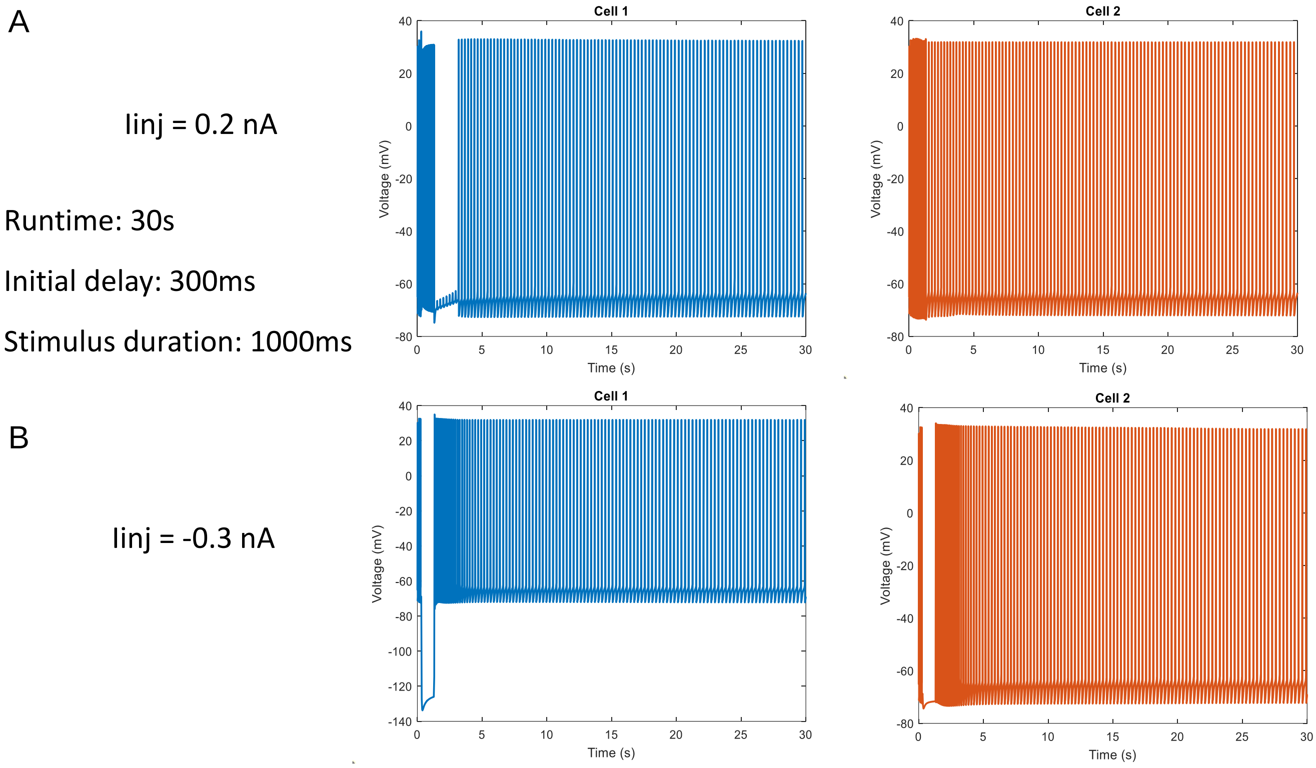

Figure 3.10: Illustration of current injection in cell 1 and its effect on spike synchrony in two-cell network during and after current injection

The time difference between two adjacent spikes in cell 1 and cell 2 decreases with time i.e., the cells resynchronize. For positive current injection, we see a after depolarisation silence following which the two cells fire together to reduce the time difference between their adjacent spikes (**Figure 3.10A**). This trend is observed for GJs present in all the three compartments but synchronization is the fastest in the case of GJ present in basal dendrite and slowest for GJ present in apical dendrite (**Figure 3.11**). The first spike after current injection of 0.2 nA for GJs present in different compartments are as follows: apical-apical GJ – 3.19022 s, basal-basal GJ – 1.92373 s and soma-soma GJ – 3.5659 s. For hyperpolarising current, we see a post inhibitory rebound following which the two cells again fire together to reduce the time difference between their consecutive spikes (**Figure 3.10B**). The time difference between consecutive spikes of cell 1 and cell 2 almost remains constant for GJ present in basal dendrite. We observe an initial increase in time difference between consecutive spikes for GJs in apical and basal dendrites because of high desynchronization due to post inhibitory rebound (**Figure 3.12**). The time difference gradually decreases with subsequent spikes and goes below to that of basal dendrites. The first spike after current injection of -0.3 nA for GJs present in different compartments are as follows: apical-apical GJ – 1.32815 s, basal-basal GJ – 1.32868 s and soma-soma GJ – 1.32783 s.

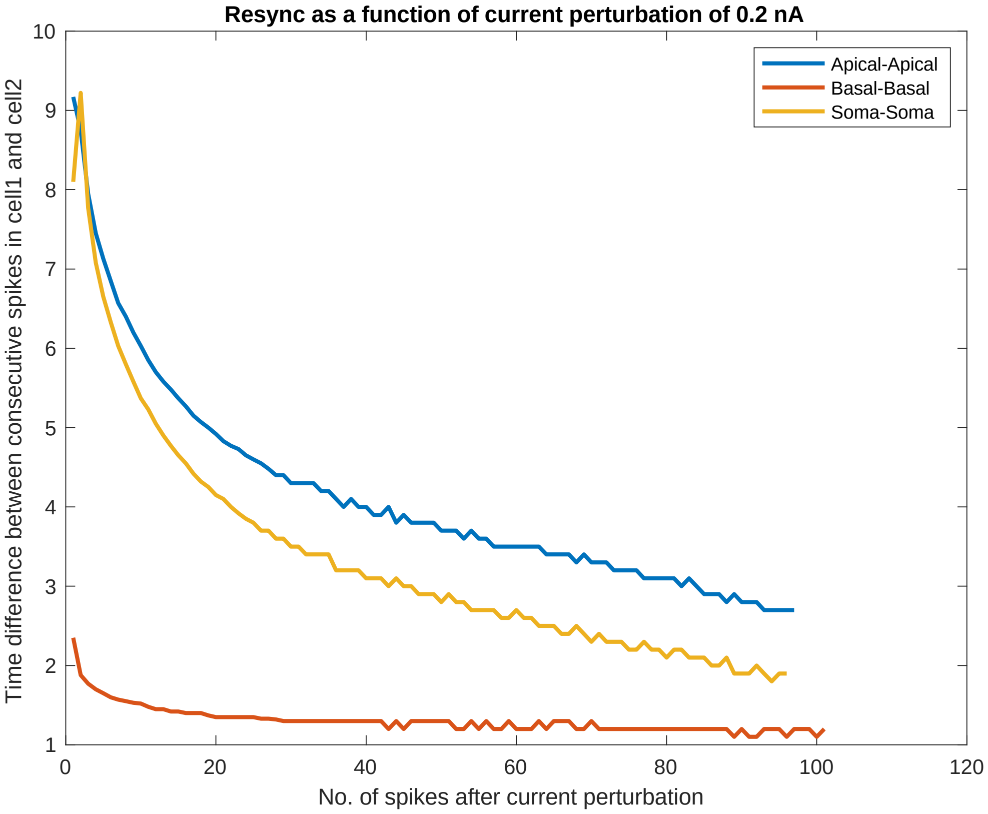

Figure 3.11: Resynchronisation of spontaneous firing in the two-cell network after current injection of 0.2 pA in cell 1.

For the above experiments, one can infer that the resynchronization time of two cells could be a function of the compartment in which the GJ is expressed due to the property of ion channels present in that compartment, it can either make resynchronization much faster of much slower.

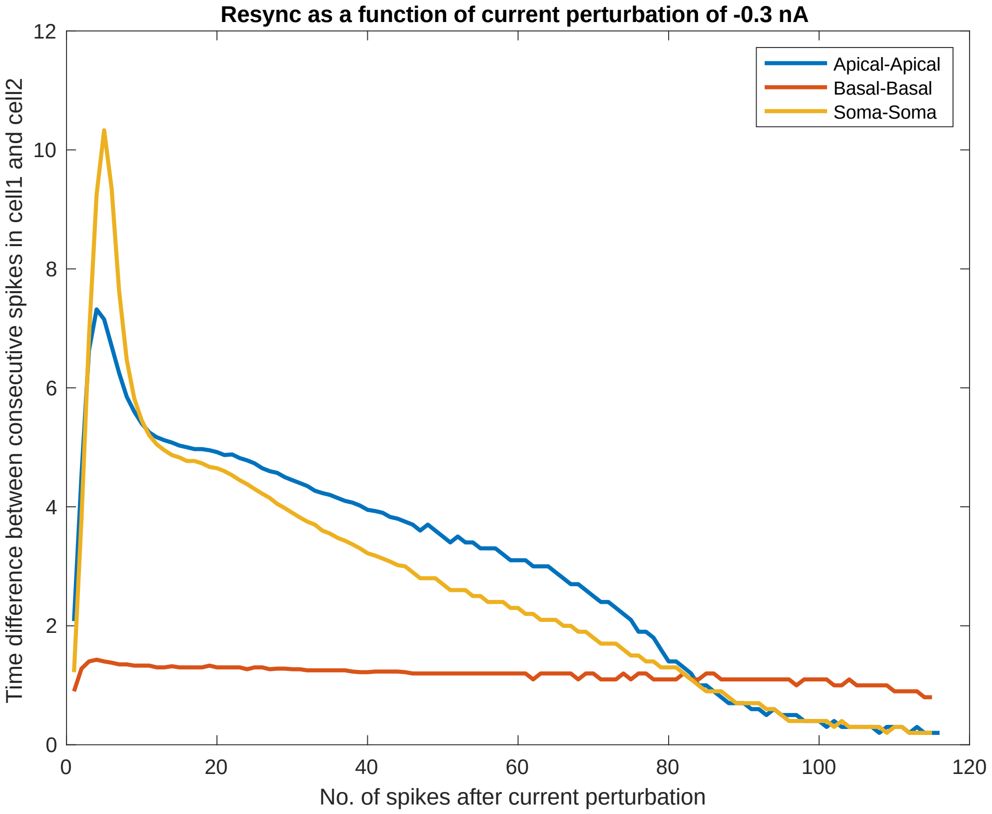

Figure 3.12: Resynchronisation of spontaneous firing in the two-cell network after current injection of -0.3 pA in cell 1.

Chapter 4: Discussion

The main finding of this study is the manifestation of degeneracy in the emergence of characteristic physiological traits of cerebellar GoC neurons. The concept of degeneracy was observed across various facets, encompassing passive characteristics and ion-channel distributions, and functionally, it encompassed multiple sub- and supra-threshold attributes of cerebellar GoC neurons. We reached this conclusion by employing an impartial stochastic search algorithm that explored 40 parameters linked to biophysically constrained models of both active and passive components of GoC. We validated the results of these stochastically generated models against 14 distinct physiological characteristics of cerebellar GoC neurons. Through this validation process, we obtained a diverse population of cerebellar GoCs that displayed cellular-scale degeneracy, showing minimal pairwise correlations among the parameters that governed these models. We used these models to illustrate the differential and variable dependencies of measurements on underlying channels. Additionally, we demonstrated that the relationship between channels and measurements was not one-to-one but rather many-to-many. Ultimately, we utilized this electrophysiologically validated model population to study the two-cell GoC network to try to uncover the mechanisms behind multidimensional population activity of electrically coupled GoC network as shown in literature.

Using chirp signal of constant amplitude, we computed impedance profile of signal being transferred to the next cell through GJ. We saw that the signals passing through GJs undergo lowpass filtering due to RC property of the membrane. This filtering is dependent upon the compartment (i.e., conductance of ion channels expressed in the compartment and its dimensions) being traversed by the signal. Signal being transferred to the next cell through GJs also show resonance at around 2 Hz. We hypothesize that, this property where signals passing through GJs undergoes low pass filtering and shows resonance at low frequency can be evoked to explain the multidimensional population activity to electrically coupled GoC network. Low pass filtering creates a virtual compartment where distinct activity of higher frequency can be confined to a subset of GoCs, thus explaining the distributed modes seen within the network. Whereas, the transfer resonance at low frequency could explain the network wide common mode. We also saw that after current perturbation the two-cell network took time to come to sync again, this could explain why the common mode manifest at slower timescales. This however does not explain why the distributed mode operates at faster timescales. Also, this only shows that common mode can occur only with low frequency signals and distributed modes can occur only with high frequency signals. Further studies are needed to comment upon occurrence of common mode with high frequency signals and of distributed modes with low frequency signals. Magnitude of transfer of signal through GJ is also dependent upon the location and conductance of GJs. As show in the above studies, strength of the signal transferred to the next cell also depends upon the compartment from which it is being transferred, which is the property of ion channels present in that compartment.

All the data is shown here is for one example case with 2 identical GoCs connected to form a network. To incorporate the effects of heterogeneity, one should also do the above experiments with other GoCs (two different identical GoCs forming a network – cell A connected with cell A, and two distinct GoCs to make a heterogenous network – cell B connected with cell B) as well. Most importantly the above hypothesis should be checked in a more realistic setup with heterogenous network with anatomical cell density in rodents with afferent inputs from MFs and GrCs and feedback output to GrCs.

Though preliminary the above results, combined with previous literature on importance of strength and variability of GJs in spike synchrony in a network, give an insight on what could be a possible mechanism behind the multidimensional population activity of electrically coupled network of GoCs which plays a key role in pattern separation and temporal processing functions attributed to GrC layer.

References:

Afshari, FS, Ptak, K, Khaliq, ZM, Grieco, TM, Slater, NT, McCrimmon, DR, and Raman, IM (2004). Resurgent Na currents in four classes of neurons of the cerebellum. J Neurophysiol 92, 2831–2843.

Albus, JS (1971). A theory of cerebellar function. Mathematical Biosciences 10, 25–61.

Aldrich, RW, Corey, DP, and Stevens, CF (1983). A reinterpretation of mammalian sodium channel gating based on single channel recording. Nature 306, 436–441.

Anirudhan, A, and Narayanan, R (2015). Analogous synaptic plasticity profiles emerge from disparate channel combinations. J Neurosci 35, 4691–4705.

Armstrong, CM, and Bezanilla, F (1977). Inactivation of the sodium channel. II. Gating current experiments. J Gen Physiol 70, 567–590.

Barmack, NH, and Yakhnitsa, V (2008). Functions of Interneurons in Mouse Cerebellum. J Neurosci 28, 1140–1152.

Basak, R, and Narayanan, R (2018). Spatially dispersed synapses yield sharply-tuned place cell responses through dendritic spike initiation. J Physiol 596, 4173–4205.

Basak, R, and Narayanan, R (2020). Robust emergence of sharply tuned place-cell responses in hippocampal neurons with structural and biophysical heterogeneities. Brain Struct Funct 225, 567–590.

Bezanilla, F, and Armstrong, CM (1977). Inactivation of the sodium channel. I. Sodium current experiments. J Gen Physiol 70, 549–566.

Brickley, SG, Cull-Candy, SG, and Farrant, M (1996). Development of a tonic form of synaptic inhibition in rat cerebellar granule cells resulting from persistent activation of GABAA receptors. J Physiol 497, 753–759.

Carnevale, NT, and Hines, ML (2006). The NEURON Book, Cambridge University Press.

Cayco-Gajic, NA, and Silver, RA (2019). Re-evaluating Circuit Mechanisms Underlying Pattern Separation. Neuron 101, 584–602.

Cesana, E, Pietrajtis, K, Bidoret, C, Isope, P, D’Angelo, E, Dieudonné, S, and Forti, L (2013). Granule Cell Ascending Axon Excitatory Synapses onto Golgi Cells Implement a Potent Feedback Circuit in the Cerebellar Granular Layer. J Neurosci 33, 12430–12446.

Chan-Palay, V, and Palay, SL (1971). The synapse en marron between Golgi II neurons and mossy fibers in the rat's cerebellar cortex. Z Anat Entwickl Gesch 133, 274–287.

Crook, JD, Hendrickson, A, Erickson, A, Possin, D, and Robinson, FR (2007). Purkinje cell axon collaterals terminate on Cat-301+ neurons in *Macaca* monkey cerebellum. Neuroscience 149, 834–844.

D‘Angelo, E, Solinas, S, MAPELLI, J, Gandolfi, D, Mapelli, L, and Prestori, F (2013). The cerebellar Golgi cell and spatiotemporal organization of granular layer activity. Frontiers in Neural Circuits 7.

Das, A, Rathour, RK, and Narayanan, R (2017). Strings on a Violin: Location Dependence of Frequency Tuning in Active Dendrites. Front Cell Neurosci 11.

Dieudonné, S (1998). Submillisecond kinetics and low efficacy of parallel fibre-Golgi cell synaptic currents in the rat cerebellum. J Physiol 510, 845–866.

Dieudonné, S, and Dumoulin, A (2000). Serotonin-Driven Long-Range Inhibitory Connections in the Cerebellar Cortex. J Neurosci 20, 1837–1848.

Dugué, GP, Brunel, N, Hakim, V, Schwartz, E, Chat, M, Lévesque, M, Courtemanche, R, Léna, C, and Dieudonné, S (2009). Electrical Coupling Mediates Tunable Low-Frequency Oscillations and Resonance in the Cerebellar Golgi Cell Network. Neuron 61, 126–139.

Eccles, JC, Llinás, R, and Sasaki, K (1966). The mossy fibre-granule cell relay of the cerebellum and its inhibitory control by Golgi cells. Exp Brain Res 1, 82–101.

Edelman, GM, and Gally, JA (2001). Degeneracy and complexity in biological systems. Proceedings of the National Academy of Sciences 98, 13763–13768.

Edgley, SA, and Lidierth, M (1987). The discharges of cerebellar Golgi cells during locomotion in the cat. J Physiol 392, 315–332.

Fink, M, and Noble, D (2009). Markov models for ion channels: versatility versus identifiability and speed. Philosophical Transactions of the Royal Society A: Mathematical, Physical and Engineering Sciences 367, 2161–2179.

Forti, L, Cesana, E, Mapelli, J, and D'Angelo, E (2006). Ionic mechanisms of autorhythmic firing in rat cerebellar Golgi cells. J Physiol 574, 711–729.

Foster, WR, Ungar, LH, and Schwaber, JS (1993). Significance of conductances in Hodgkin-Huxley models. Journal of Neurophysiology 70, 2502–2518.

Geurts, FJ, Timmermans, J, Shigemoto, R, and De Schutter, E (2001). Morphological and neurochemical differentiation of large granular layer interneurons in the adult rat cerebellum. Neuroscience 104, 499–512.

Goaillard, J-M, and Marder, E (2021). Ion Channel Degeneracy, Variability, and Covariation in Neuron and Circuit Resilience. Annu Rev Neurosci 44, 335–357.

Goldman, MS, Golowasch, J, Marder, E, and Abbott, LF (2001). Global Structure, Robustness, and Modulation of Neuronal Models. J Neurosci 21, 5229–5238.

Gurnani, H, and Silver, RA (2021). Multidimensional population activity in an electrically coupled inhibitory circuit in the cerebellar cortex. Neuron 109, 1739-1753.e8.

Heine, SA, Highstein, SM, and Blazquez, PM (2010). Golgi Cells Operate as State-Specific Temporal Filters at the Input Stage of the Cerebellar Cortex. J Neurosci 30, 17004–17014.

Hemond, P, Migliore, M, Ascoli, GA, and Jaffe, DB (2009). The membrane response of hippocampal CA3b pyramidal neurons near rest: heterogeneity of passive properties and the contribution of hyperpolarization-activated currents. Neuroscience 160, 359–370.

Holtzman, T, Rajapaksa, T, Mostofi, A, and Edgley, SA (2006). Different responses of rat cerebellar Purkinje cells and Golgi cells evoked by widespread convergent sensory inputs. J Physiol 574, 491–507.

Ito, M (2013). Error detection and representation in the olivo-cerebellar system. Front Neural Circuits 7.

Ito, M, Yamaguchi, K, Nagao, S, and Yamazaki, T (2014). Long-term depression as a model of cerebellar plasticity. Prog Brain Res 210, 1–30.

Jain, A, and Narayanan, R (2020). Degeneracy in the emergence of spike-triggered average of hippocampal pyramidal neurons. Sci Rep 10, 374.

Jakab, RL, and Hámori, J (1988). Quantitative morphology and synaptology of cerebellar glomeruli in the rat. Anat Embryol (Berl) 179, 81–88.

van Kan, PL, Gibson, AR, and Houk, JC (1993). Movement-related inputs to intermediate cerebellum of the monkey. J Neurophysiol 69, 74–94.

Kanichay, RT, and Silver, RA (2008). Synaptic and Cellular Properties of the Feedforward Inhibitory Circuit within the Input Layer of the Cerebellar Cortex. J Neurosci 28, 8955–8967.

Leiner, HC, Leiner, AL, and Dow, RS (1986). Does the cerebellum contribute to mental skills? Behav Neurosci 100, 443–454.

Marder, E, and Taylor, AL (2011). Multiple models to capture the variability in biological neurons and networks. Nat Neurosci 14, 133–138.

Marr, D (1969). A theory of cerebellar cortex. The Journal of Physiology 202, 437–470.

Masoli, S, Ottaviani, A, Casali, S, and D'Angelo, E (2020). Cerebellar Golgi cell models predict dendritic processing and mechanisms of synaptic plasticity. PLoS Comput Biol 16, e1007937.

Migliore, R, Lupascu, CA, Bologna, LL, Romani, R, Courcol, J-D, Antonel, S, Van Geit, WAH, Thompson, AM, Mercer, A, Lange, S, *et al.* (2018). The physiological variability of channel density in hippocampal CA1 pyramidal cells and interneurons explored using a unified data-driven modeling workflow. PLOS Computational Biology 14.

Mishra, P, and Narayanan, R (2019). Disparate forms of heterogeneities and interactions among them drive channel decorrelation in the dentate gyrus: Degeneracy and dominance. Hippocampus 29, 378–403.

Mishra, P, and Narayanan, R (2021). Ion-channel degeneracy: Multiple ion channels heterogeneously regulate intrinsic physiology of rat hippocampal granule cells. Physiol Rep 9, e14963.

Mittal, D, and Narayanan, R (2018). Degeneracy in the robust expression of spectral selectivity, subthreshold oscillations, and intrinsic excitability of entorhinal stellate cells. J Neurophysiol 120, 576–600.

Mukunda, CL, and Narayanan, R (2017). Degeneracy in the regulation of short-term plasticity and synaptic filtering by presynaptic mechanisms. J Physiol 595, 2611–2637.

Narayanan, R, and Johnston, D (2007). Long-term potentiation in rat hippocampal neurons is accompanied by spatially widespread changes in intrinsic oscillatory dynamics and excitability. Neuron 56, 1061–1075.

Narayanan, R, and Johnston, D (2008). The h channel mediates location dependence and plasticity of intrinsic phase response in rat hippocampal neurons. J Neurosci 28, 5846–5860.

Oberdick, J, and Sillitoe, RV (2011). Cerebellar zones: history, development, and function. Cerebellum 10, 301–306.

Palay, SL, and Chan-Palay, V (1974). Cerebellar Cortex: Cytology and Organization, Springer.

Pijpers, A, Apps, R, Pardoe, J, Voogd, J, and Ruigrok, TJH (2006). Precise Spatial Relationships between Mossy Fibers and Climbing Fibers in Rat Cerebellar Cortical Zones. The Journal of Neuroscience 26, 12067.

Prestori, F, Mapelli, L, and D’Angelo, E (2019). Diverse Neuron Properties and Complex Network Dynamics in the Cerebellar Cortical Inhibitory Circuit. Front Mol Neurosci 12.

Prinz, AA, Billimoria, CP, and Marder, E (2003). Alternative to hand-tuning conductance-based models: construction and analysis of databases of model neurons. J Neurophysiol 90, 3998–4015.

Prinz, AA, Bucher, D, and Marder, E (2004). Similar network activity from disparate circuit parameters. Nat Neurosci 7, 1345–1352.

Prsa, M, Dash, S, Catz, N, Dicke, PW, and Thier, P (2009). Characteristics of Responses of Golgi Cells and Mossy Fibers to Eye Saccades and Saccadic Adaptation Recorded from the Posterior Vermis of the Cerebellum. J Neurosci 29, 250–262.

Purves et al. (2018), 6th ed. Neuroscience, Oxford University Press USA, Chapter 16

Purves et al. (2018), 6th ed. Neuroscience, Oxford University Press USA, Chapter 20

Rathour, RK, Malik, R, and Narayanan, R (2016). Transient potassium channels augment degeneracy in hippocampal active dendritic spectral tuning. Sci Rep 6, 24678.

Rathour, RK, and Narayanan, R (2012). Inactivating ion channels augment robustness of subthreshold intrinsic response dynamics to parametric variability in hippocampal model neurons. J Physiol 590, 5629–5652.

Rathour, RK, and Narayanan, R (2014). Homeostasis of functional maps in active dendrites emerges in the absence of individual channelostasis. Proceedings of the National Academy of Sciences 111, E1787–E1796.

Rathour, RK, and Narayanan, R (2019). Degeneracy in hippocampal physiology and plasticity. Hippocampus 29, 980–1022.

Roš, H, Sachdev, RNS, Yu, Y, Šestan, N, and McCormick, DA (2009). Neocortical Networks Entrain Neuronal Circuits in Cerebellar Cortex. J Neurosci 29, 10309–10320.

Rossi, DJ, and Hamann, M (1998). Spillover-mediated transmission at inhibitory synapses promoted by high affinity alpha6 subunit GABA(A) receptors and glomerular geometry. Neuron 20, 783–795.

Roy, A, and Narayanan, R (2021). Spatial information transfer in hippocampal place cells depends on trial-to-trial variability, symmetry of place-field firing, and biophysical heterogeneities. Neural Netw 142, 636–660.

Seenivasan, P, and Narayanan, R (2020). Efficient phase coding in hippocampal place cells. Phys Rev Res 2, 033393.

Shridhar, S, Mishra, P, and Narayanan, R (2022). Dominant role of adult neurogenesis-induced structural heterogeneities in driving plasticity heterogeneity in dentate gyrus granule cells. Hippocampus 32, 488–516.

Simat, M, Parpan, F, and Fritschy, J-M (2007). Heterogeneity of glycinergic and gabaergic interneurons in the granule cell layer of mouse cerebellum. J Comp Neurol 500, 71–83.

Sinha, M, and Narayanan, R (2022). Active Dendrites and Local Field Potentials: Biophysical Mechanisms and Computational Explorations. Neuroscience 489, 111–142.

Solinas, S, Forti, L, Cesana, E, Mapelli, J, De Schutter, E, and D‘Angelo, E (2007a). Computational reconstruction of pacemaking and intrinsic electroresponsiveness in cerebellar golgi cells. Front Cell Neurosci 1.

Solinas, S, Forti, L, Cesana, E, Mapelli, J, De Schutter, E, and D‘Angelo, E (2007b). Fast-reset of pacemaking and theta-frequency resonance patterns in cerebellar golgi cells: Simulations of their impact in vivo. Front Cell Neurosci 1.

Solinas, S, Nieus, T, and D’Angelo, E (2010). A realistic large-scale model of the cerebellum granular layer predicts circuit spatio-temporal filtering properties. Front Cell Neurosci 4, 12.

Srikanth, S, and Narayanan, R (2015). Variability in State-Dependent Plasticity of Intrinsic Properties during Cell-Autonomous Self-Regulation of Calcium Homeostasis in Hippocampal Model Neurons,,. eNeuro 2, ENEURO.0053-15.2015.

Szoboszlay, M, Lőrincz, A, Lanore, F, Vervaeke, K, Silver, RA, and Nusser, Z (2016). Functional Properties of Dendritic Gap Junctions in Cerebellar Golgi Cells. Neuron 90, 1043–1056.

Taylor, AL, Goaillard, J-M, and Marder, E (2009). How multiple conductances determine electrophysiological properties in a multicompartment model. J Neurosci 29, 5573–5586.

TED (2011). Daniel Wolpert: The real reason for brains.

Varghese, A, and Boland, LM (2002). Computing transient gating charge movement of voltage-dependent ion channels. J Comput Neurosci 12, 123–137.

Vervaeke, K, Lőrincz, A, Gleeson, P, Farinella, M, Nusser, Z, and Silver, RA (2010). Rapid Desynchronization of an Electrically Coupled Interneuron Network with Sparse Excitatory Synaptic Input. Neuron 67, 435–451.

Vos, BP, Volny-Luraghi, A, and De Schutter, E (1999). Cerebellar Golgi cells in the rat: receptive fields and timing of responses to facial stimulation. Eur J Neurosci 11, 2621–2634.

Watanabe, D, and Nakanishi, S (2003). mGluR2 Postsynaptically Senses Granule Cell Inputs at Golgi Cell Synapses. Neuron 39, 821–829.

Witter, L, Rudolph, S, Pressler, RT, Lahlaf, SI, and Regehr, WG (2016). Purkinje Cell Collaterals Enable Output Signals from the Cerebellar Cortex to Feed Back to Purkinje Cells and Interneurons. Neuron 91, 312–319.

Xu, W, and Edgley, SA (2008). Climbing fibre-dependent changes in Golgi cell responses to peripheral stimulation. J Physiol 586, 4951–4959.

Xu-Friedman, MA, and Regehr, WG (2003). Ultrastructural Contributions to Desensitization at Cerebellar Mossy Fiber to Granule Cell Synapses. J Neurosci 23, 2182–2192.